PAPER

Statistically representative estimators of multi-scale surface topography: example of aluminum blasted rough samples

To cite this article: C Turbil *et al* 2023 *Surf. Topogr.: Metrol. Prop.* **11** 025018

View the article online for updates and enhancements.

Surface Topography: Metrology and Properties

PAPER

Statistically representative estimators of multi-scale surface topography: example of aluminum blasted rough samples

C Turbil[1], J Cabrero[2] ⓘ, I Simonsen[1,3] ⓘ, D Vandembroucq[4] ⓘ and I Gozhyk[1] ⓘ

[1] SVI, UMR 125 CNRS/Saint-Gobain Research Paris, 39 quai Lucien Lefranc, F-93303 Aubervilliers, France
[2] Saint-Gobain Research Provence, 550 avenue Alphonse Jauffret, F-84306 Cavaillon, France
[3] Department of Physics, NTNU—Norwegian University of Science and Technology, NO-7491 Trondheim, Norway
[4] PMMH, CNRS, ESPCI Paris, PSL University, Sorbonne Universté, Université de Paris, 10 rue Vauquelin, F-75231 Paris cedex 05, France

E-mail: iryna.gozhyk@saint-gobain.com

Abstract

The topography of a rough surface determines many of its physical properties, for instance, tribology, contact mechanics, optical properties etc. Nowadays, a deep understanding of such physical phenomena requires the knowledge of the topography at appropriate length scales. Apart from performing multi-scale measurements of the surface topography, it also requires the use of proper statistical estimators for the analysis of such topography maps. Moreover, when dealing with light scattering in the visible spectral range, the scale at which the estimators of local topography properties are defined is extremely important. Here we present a multi-scale and statistical study of the surface topography of blasted aluminum samples which all have rather different visual appearance. Various statistical estimators of surface topography are examined, including estimators related to the height distribution, the lateral correlation and local topology. The combination of these various estimators unveils a scale separation between a micro-scale roughness inherited from the initial cold-rolled aluminum surface and a large scale roughness fully controlled by the blasting process. A special emphasis is given to the crucial importance of length scales in the estimation of local slopes. The present analysis establishes a quantitative link between the statistical properties of the surface topography and the blasting process used to fabricate the samples.

1. Introduction

Surface morphology influences many physical processes taking place at, or close to, the surface of objects. Therefore, interesting functional properties can be added to the surface through thoroughly controlled topography, for example, hydrophobicity [1], friction [2] and adhesion [3], hazy or glossy appearance governed by light scattering [4]. Furthermore, nowadays the aesthetics of an object is an important criteria for the development of industrial products, even if their primary function has nothing to do with optics. Surface topography can also deteriorate mechanical and electrical properties, as for instance the variation of contact stiffness with the true area of contact at interface [5, 6].

The impact of the morphology of randomly rough surfaces on their optical properties has been in the focus of physical optics since the 1900s [7, 8]. In the small roughness limit, also referred to as *smooth surface* limit, a unique analytic solution exists, known as the Rayleigh-Rice vector perturbation theory model [4, 7], and allows one to directly link optical properties of the surface to the statistical properties of its surface morphology [4]. Thorough morphological and optical studies [9–11] of random surfaces exhibiting small roughness proved the applicability of the Rayleigh-Rice theory to real life surfaces of various origin [4]. On the other hand, if the surface roughness is moderately large compared to the wavelength of illumination, light scattering at small angles by samples while illuminated at small incidence angles, can be described with the Kirchhoff model [4]. In other cases, no general analytical model is available and the use of direct numerical solution of Maxwell equations for given surface morphology remains the only general approach.

To some extent, the moderately large and large roughness cases can be approximately treated with

geometrical optics laws. Such a phenomenological approach, the microfacet theory, was introduced in 1963 [12] and adopted in early 1970s by the computer graphics community [13, 14] for the physico-realistic rendering. In this approach the surfaces are seen as ensembles of micrometer-scale facets and light scattering is described through the statistics of facet orientations with respect to the macroscopic surfaces. The 3D distribution of scattered light is then used to create a virtual image of the object. Since the microfacet theory was introduced [12], numerous models have been developed which are able to fit various 3D distributions of scattered light of real surfaces [13–18]. Today an untrained eye can seldom recognize the virtual reality image. Yet, existing rendering tools should still be developed further in order to account for light polarization [19] and diffraction-related effects [20, 21] that are observed in real life.

Interestingly, in contrast to the small roughness case, very few thorough studies of surface morphology have been reported for the moderately large and large roughness cases, probably due to the necessity of a multi-scale surface analysis. Therefore, strong assumptions on surface statistics were made in both physical optics and computer graphics models. For instance, both approaches rely on the assumption that rough surfaces follow Gaussian statistics. Although this hypothesis is widely used, it remains unclear to which extent real-world surfaces with spatial frequencies at sub-milimeter scale exhibit Gaussian statistics. More importantly, in contrast to the case of physical optics [9, 10, 12, 22], the achievement of a quantitative link between surface roughness characterization and scattering properties in the framework of micro-facets models remains elusive. It should be mentioned that measured angular light intensity distributions scattered from randomly rough surfaces were recently used to successfully predict the statistical properties of a broad class of rough surfaces using several physical optics approaches [23, 24].

It was found in the 2000s that even for surfaces with prominent micro-scale roughness the nano-scale component can significantly impact the physical properties [2], for example, the super-hydrophobicity for which the lotus leaf is a classic natural example [1] requires a combined micro- and nano-scale roughness. Prominent nano-scale roughness can also alter the optical properties of surfaces with micro-scale roughness. In order to address this problem from the experimental side, not only angle-resolved scattering experiments are necessary but also detailed knowledge of the surface topography is required.

The scope of this paper is to address these questions through a thorough analysis of the topography of micro-scale rough surfaces with notable difference in visual appearance. Blasting technique was chosen for sample fabrication due to its inherent versatility in terms of treatable materials and ability to alter the surface topography [25–29], and as a result the electrical

[5, 6], mechanical [5, 6, 30] and optical properties of the sample. For instance, blasting can provide very different finish [31] and thereby aesthetics to the same bare surface. The micro-topography induced by blasting process depends on the plastic properties of the material composing the surface as well as on the material and shape of the blasting medium [32, 33]. In the case of aluminum, plastic deformation often takes place [26]. The surface erosion depends on material ductility [34], the angle of incidence [35] and other parameters such as size and shape of blasting media [33]. Surface blasting is often considered a random process since it is produced by a large number of random independent impact events [36].

Numerous papers reported surface topography studies of blasted surfaces [25–28, 33, 35, 37, 38]. Yet, very few publications contained topography data measured at different scales [28], and moreover statistical topography parameters analyzed in previous studies often focused on arithmetical mean (Ra) or root-mean square (rms also known as Rq) deviations [25–27] and seldom other parameters such as curvature [38] or apparent slopes [37] and even less auto-correlation function or power spectral density. In this study we focus on several surface estimators which are essential for the analysis of optical properties and linking them to the fabrication process. A more exhaustive list of surface estimators reported to be used on multi-scale analysis of surface topography can be found in [36, 39–42], in particular on less widespread techniques to estimate lateral correlations (wavelet and modal analysis) as well as closing and opening morphological filters [42, 43].

This paper presents a thorough multi-scale study of the morphology of blasted aluminum plates. Section 2 provides the details on fabrication and visual assessment of samples examined in this work. The second part of section 2 describes how the statistically representative topography data of those samples were gathered from three different experimental setups. Section 3 introduces the statistical aspects of the analysis of morphology of randomly rough surfaces. Sections 4–7 focus on morphology parameters related to height distribution, spatial correlations, surface slopes and local topology respectively. The analysis of statistical parameters of surface morphology given in sections 4–7 allow to understand how the morphology of the surfaces is being modified through blasting. And last but not the least, provided analysis allows to establish a link between the micro-scale features of examined surfaces and parameters of fabrication process.

2. Materials and methods

2.1. Fabrication and description of samples
The samples that we will be concerned with in this work are four 5×5 cm^2 aluminum (6061) plates treated by different industrial processes. Figure 1
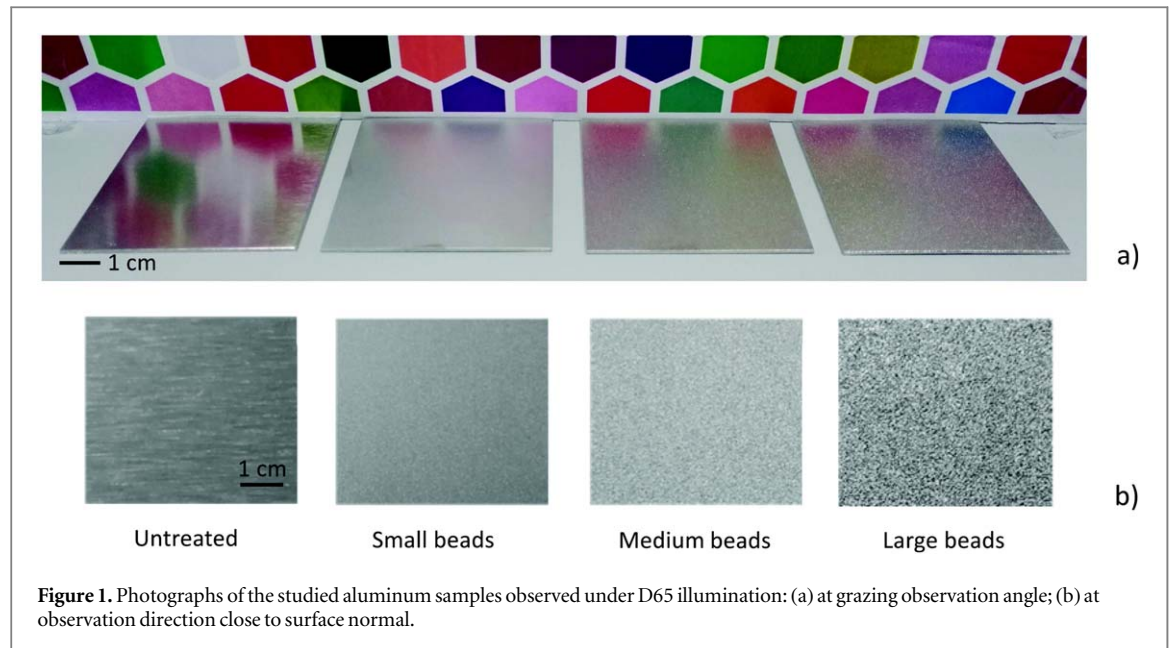
Figure 1. Photographs of the studied aluminum samples observed under D65 illumination: (a) at grazing observation angle; (b) at observation direction close to surface normal.

provides photographs of all four samples taken in a light booth (Spectralight QC X-Rite) under controlled illumination (D65 illumination). The photos taken at grazing observation angle are shown in figure 1(a), while macro photos taken close to the surface normal are presented in figure 1(b).

The first sample is a cold rolled aluminum plate which we hereafter will refer to as the *untreated* sample. From figure 1 it clearly appears that this untreated sample is strikingly anisotropic. The direction of the grooves of the surface coincides with the rolling direction used during the manufacturing. The surface roughness of cold-rolled aluminum is known to exhibit self-affine surface statistics [44, 45]. Many natural and machined fault surfaces exhibit self-affinity within at least several decades of spatial frequencies. Some recent works suggest that the self-affinity can be produced during adhesive wear due to the interplay between brittle and ductile mechanisms [46]. The remaining three samples were fabricated from such cold rolled aluminum plates (untreated samples) by blasting them by ceramic beads of different sizes; in the following, these bead sizes will be referred to as *small*, *medium* or *large* beads. More specifically, spherical ceramic beads commercialized by ZirPro were used in the blasting process. Their average diameters of the beads were $70 \pm 20\,\mu$m (small), $200 \pm 50\,\mu$m (medium), and $500 \pm 150\,\mu$m (large). The uncertainties reported on these numbers are the full-width at half maximum (FWHM) of the respective diameter distributions. The blasting process was performed in an air suction blasting machine at normal incidence to the mean surface of the sample. The pressure of the venturi type blasting source was 2 bar, and each of the samples were blasted for 50 s, twice the time necessary to completely cover the surface with blasting impacts.

The four samples have rather different visual appearances. The untreated sample looks very glossy at grazing angle (figure 1(a)). In contrast, the three blasted samples have completely different visual aspects. For instance, they appear significantly less glossy at grazing angles (figure 1(a)). Meanwhile, their gloss seems to be different, which is in agreement with the apparent differences in the morphology of the blasted samples seen on the photographs in figure 1(b). From these figures several observations should be made. First, the change in apparent grain size from small to large (figure 1(b)) is consistent with the size of the beads used in the blasting process (smallest grains in the case of treatment by small beads and largest grains for the large beads). Second, the blasting process reduces the degree of anisotropy of the resulting surfaces relative to the surface of the untreated sample. To the naked eye, the blasted surfaces appear to be almost isotropic; these observations we will later confirm when performing the detailed analysis of the measured surface morphologies.

2.2. Description of topography measurements

In order to provide a multi-scale analysis of the surface morphology, the interfaces of all four samples were measured by three different experimental setups exploiting different measurement principles and covering different ranges of spatial frequencies: an optical profilometer (a chromatic confocal sensor, CCS Prima, STIL), and two scanning probe profilometers, where the first is a stylus profilometer (Dektak XT, Bruker) and the second an atomic force microscope (AFM, Icon, Bruker). The optical profilometer provides a non-contact scan, and the surface height is determined from optical coherence of the wide-spectrum probe light reflected by the surface. In the case of scanning probe profilometers the surface scan is performed by a solid tip and the surface height is defined from tip deflection (in AFM a nano-tip is used). Surface topography analysis performed with

Table 1. Summary of the parameters assumed in performing the topography measurements.* 1D scans were performed in two orthogonal directions for each of the 25 examined locations.

	Map	Sample	L[mm]	N	Δ[μm]	D[μm]	δ_h[nm]	# maps
Optical profilometer	2D	Untreated	5	2501	2	2	300	8
		Small beads	1	501				9
		Medium beads	2	1001				8
		Large beads	3	1501				6
Stylus profilometer	1D	Untreated	6	60001	0.1	10	10	25*
		Small beads	6	60001	0.1			20*
		Medium beads	15	75001	0.2			20*
		Large beads	15	45001	0.33			25*
AFM	2D	Untreated	0.02	512	0.02	0.04	2	4
		Blasted	0.03	512	0.06			3

setups covering different but overlapping ranges of spatial frequencies also allows avoiding the measurement-related variation of estimators [47].

The *surface profile function* $z = h(\mathbf{r})$ was obtained from such measurements. Here we have defined a coordinate system where the mean surface, assumed to be planar, coincides with the plane $z = 0$ and the positive z-axis is pointing upward. The vector $\mathbf{r} = (x, y)$ denotes an arbitrary in-plane position vector. Furthermore, the in-plane orientation of the coordinate system is chosen so that the unit vector $\mathbf{e}_x = (1, 0)$ coincides with the rolling direction used when producing the untreated sample. In other words, the x-axis of the coordinate system is parallel to the grooves of the untreated samples like the one presented in e.g. figure 1(b).
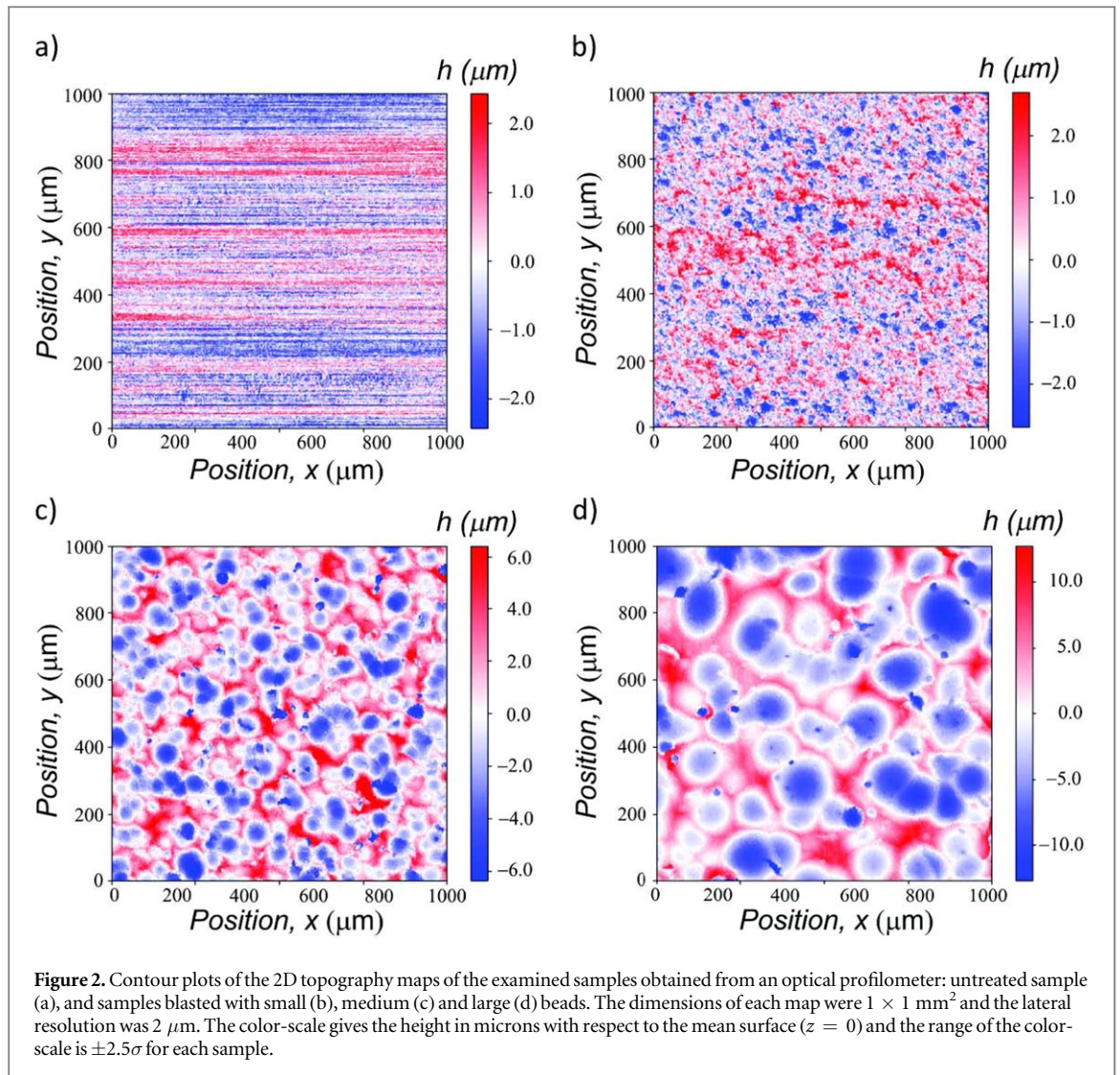
With the use of optical profilometer and an AFM the two-dimensional (2D) surface morphology of the samples were measured at the set of $N \times N$ points $\{h(x_{n_x}, y_{n_y})\}$ with a measurement step Δ, corresponding to a rectangular grid in a square region of area $L \times L$ of the mean plane ($z = 0$) covered by the rough surface. The values of L, Δ and N used in performing these measurements are summarized in table 1. This table also provides information on minimum resolvable height variation δ_h and the diameter D of the measurement element. The latter stands for the tip diameter in case of AFM and stylus profilometer and the diameter of light spot produced by the optical pencil in the optical profilometer. These values are large compared to the uncertainty of the displacement of the precision motors used in these setups and provide more realistic estimates of the high-frequency cut-offs for the horizontal displacements. Moreover, the finite diameter of the stylus tip does imply a high-frequency cut-off. The latter depends on both tip diameter and surface roughness [48–50] and is especially relevant for the analysis of fractal surfaces [51, 52]. To ensure sufficient statistics, the measurements were repeated several times at different locations on the sample for each setup that was used. One-dimensional (1D) line-scan measurements were performed using a stylus profilometer. The spatial length of the each of the line-scan was L and the number of points used was N. The measurements were done either along the x or the y direction the coordinate system, and in this way we obtained $\{h(x_{n_x}, 0)\}$ or $\{h(0, y_{n_y})\}$, respectively. In measurements performed with optical and stylus profilometers the scan ranges used for each sample were chosen in such a way as to have sufficient statistics and to be sufficiently long compared to the measured correlation length of the sample [53].

3. Characterization of randomly rough surfaces

Randomly rough surfaces can be considered as realizations of an underlying random process [36, 54, 55]. Then it is customary to describe the surface roughness through various statistical estimators and probability distribution functions. The statistical analysis implies several strong assumptions on the surface profile function $h(\mathbf{r})$. The most central of these assumptions for $h(\mathbf{r})$ is that it is (i) a single-valued function of $\mathbf{r}$ that is differential with respect to x and y and constitutes an (ii) ergodic, (iii) stationary and (iv) zero-mean random process [55].

(i) Numerous real-life surfaces, including rolled and blasted surfaces, exhibit single-valued height distribution.

(ii) Statistics of random process uses the averaging over the ensemble of realizations. The ergodicity of the random process allows to equivalently interpret $\langle A \rangle$, the average of a given quantity A over the ensemble of realizations, as a *spatial average* within a single realization of the process provided the spatial average $\overline{A}$ is taken over a sufficiently large region of the mean surface. The latter interpretation of the average is the most convenient when dealing with measured data.

(iii) The stationarity condition implies here that no trend can be identified along the spatial coordinates i.e. the statistical properties of the surface

Figure 2. Contour plots of the 2D topography maps of the examined samples obtained from an optical profilometer: untreated sample (a), and samples blasted with small (b), medium (c) and large (d) beads. The dimensions of each map were 1×1 mm^2 and the lateral resolution was 2 μm. The color-scale gives the height in microns with respect to the mean surface ($z = 0$) and the range of the color-scale is $\pm 2.5\sigma$ for each sample.

roughness remain independent of the spatial region that is probed.

(iv) Finally, the experimental data are usually acquired in the coordinate system related to the measurement setup. Thereby, prior to any statistical data analysis a detrending step has to be performed to bring the height profile to a coordinate system relative to the mean sample surface. This may imply the correction of a possible systematic trend (e.g. tilt or macroscopic curvature) correction in addition of the simple deduction of the average height.

Some of these assumptions may not be respected by the real-life surfaces due to the variation in machining factors such as imperfections in treatment parameters or local fluctuations of chemical composition in materials [56, 57]. Yet statistical tools for description of a more general case remain to be developed. Therefore, the analysis provided in this paper mostly relies on these assumptions. Moreover, since the sandblasted surfaces are produced by a large number

of independent impacts [32, 33], they are generally considered randomly rough [36].

We show in figure 2 height maps measured with the optical profilometer over an area of 1×1 mm^2 in each examined sample. This series of height maps is to be compared with the series of photographs shown in figure 1. The figure illustrates that the micro-scale morphology of the aluminum plate is drastically modified by the blasting process. The anisotropy of the *untreated* sample is apparent even without any statistical data analysis, yet the blasted samples show no obvious anisotropy. The apparent graininess of the blasted samples at the macro-scale (figure 1) can be associated to the characteristic micro-scale crater-like patterns visible in the height maps (figure 2). The lateral dimension of the craters as well as their depth increase with the size of beads used in the blasting. In the following of the paper we discuss how to use different statistical estimators to give a quantitative support to these qualitative observations.

Some man-made surfaces are obtained as a sequence of surface modification steps, where the first

step provides for the coarse finish and the subsequent steps result into the refinement of the surface finish. Such surfaces are often referred to as interrupted finishes or stratified surfaces or multi-process surfaces [33, 58]. Although our examined samples were obtained within two fabrication steps, each of which impacted surface topography at different scales, they do not perfectly match the definition of multi-process surfaces as given in [36] since, as will be shown in this paper, the coarse finish was obtained by the surface blasting –the last surface treatment step.

For the sake of clarity, the analysis of the statistical descriptors given in this paper is separated in four separate sections, each focusing on a different type of statistical descriptors, similarly to amplitude, spatial, hybrid and functional parameters suggested by [41]. First, in section 4 the height distribution and related estimators are discussed. The analysis of spatial correlations are presented in section 5. Then the local slopes calculated at different scales are discussed in section 6. Finally, estimators of the local curvature are analyzed and presented in section 7. Each section briefly introduces the definitions of the statistical estimators of interest and then illustrates their use on the morphology measurements for the examined aluminum samples.

4. Height distribution

4.1. Theoretical context

A randomly rough surface and its corresponding surface profile function $h(\mathbf{r})$, can be assumed to constitute a stochastic random process [54]. A first characterization of such a process is given by the probability distribution function (pdf) of the height values, $p(h)$. This distribution gives us information about the (vertical) height fluctuations of the surface but naturally ignores the possible spatial correlations.

Because of its ubiquity and its analytical simplicity, the Gaussian (or normal) form for the height distribution function is widely used in analytical and computational studies of light scattering from rough surfaces [59]:

$$p(h) = \frac{1}{\sqrt{2\pi}\,\sigma} \exp\left[-\frac{(h - \langle h \rangle)^2}{2\sigma^2}\right], \quad (1)$$

with $\langle h \rangle = 0$. Many real-life surfaces can indeed be reasonably well approximated by Gaussian statistics, as for instance fault surfaces, surfaces obtained through blasting or ion sputtering [60]. In theory, processes like grinding are supposed to provide for Gaussian statistics as well, but due to process imperfections it is not always the case [56, 57]. However, the assumption of Gaussian statistics is definitely not applicable in the case of surfaces obtained by fracture followed by slight polishing [60] or growing interfaces with less than one monolayer of atoms [39]. In the case of Gaussian statistics the height fluctuations of the surface are fully characterized by a single scalar parameter, the height standard deviation σ i.e. root-mean-square (RMS) height (also referred to as Rq):

$$\sigma = \langle h^2(\mathbf{r})\rangle^{1/2}; \quad (2)$$

Historically, due to simplicity of calculation, another surface parameter, namely the average roughness Ra (the deviation of the surface from the mean height), was often used in experimental surface characterization. Although this parameter does not intervene in physical models, we provide it for the sake of comparison. However not all rough surfaces can accurately be described by a Gaussian height distribution, for example surfaces prepared by fracture followed by slight polishing [60]. In the non-Gaussian case, all the moments $m_n = \langle h^n(\mathbf{r})\rangle$ are theoretically required to get a full knowledge of the height distribution $p(h)$. Here $m_1 = \langle h(\mathbf{r})\rangle$ is the mean $\bar{h}$ that we set to zero by convention and $m_2 = \langle h^2(\mathbf{r})\rangle = \sigma^2$ is the variance of the height distribution (i.e. rms roughness squared). The numerical estimate of the moments of higher order is however highly dependent of the tails of the distribution. Such a characterization requires a large statistics to reduce the uncertainty on the estimated moments [61, 62]. Moreover, the associated dependence on extreme values often induces a high sensitivity to measurement artifacts [62]. For surfaces with multi-scale roughness, statistically-representative measurements should be performed at each scale of relevance for the physical properties of interest.

It is thus customary to limit the additional characterization of the height distribution to only two parameters, associated with the moments of third and forth order, respectively the skewness and the kurtosis:

- The *skewness* of the surface (γ_3) expresses the asymmetry of the height distribution with respect to the mean level (here conventionally taken as zero $\langle h \rangle = 0$). It is expressed as:

$$\gamma_3 = \frac{1}{\sigma^3}\langle h^3(\mathbf{r})\rangle; \quad (3)$$

- The *kurtosis* of a surface (γ_4), describes the tails of the distribution, and is expressed as:

$$\gamma_4 = \frac{1}{\sigma^4}\langle h^4(\mathbf{r})\rangle. \quad (4)$$

In summary, when dealing with the real-life rough surfaces, the very common assumption of Gaussian statistics should be handled with caution [36]. In addition of the computation of the RMS roughness, the estimates of the skewness and the kurtosis (whose expected values are respectively $\gamma_3 = 0$ and $\gamma_4 = 3$ for a Gaussian distribution) allow to test quantitatively the distance of the height distribution to Gaussianity. But such evaluation requires a significant amount of measured points [62].

4.2. Experimental results

Table 2 summarizes the values of the RMS, skewness and kurtosis calculated on the basis of the expressions
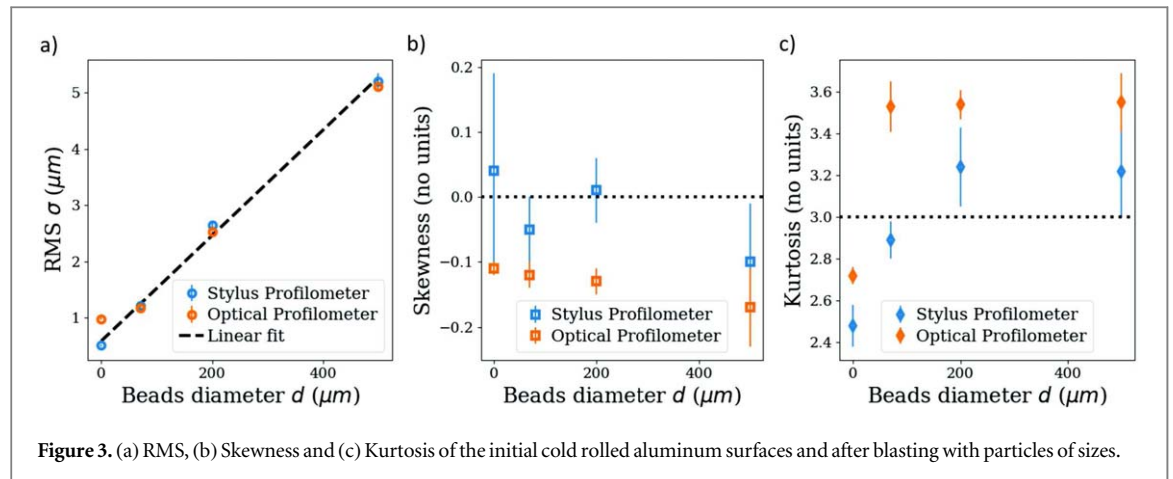
Figure 3. (a) RMS, (b) Skewness and (c) Kurtosis of the initial cold rolled aluminum surfaces and after blasting with particles of sizes.

Table 2. Statistical estimators of height distribution (RMS, skewness and kurtosis) parameters extracted from experimental characterization of blasted samples aluminum plate and reference untreated plate.

Estimator	Profilometer	Untreated sample	Small beads	Medium beads	Large beads
RMS (μm)	Optical	$0.98 \pm 0.02^*$	1.18 ± 0.04	2.52 ± 0.02	5.11 ± 0.06
	Stylus	0.51 ± 0.02	1.21 ± 0.04	2.64 ± 0.04	5.20 ± 0.14
	AFM	$0.052 \pm 0.011^*$	0.32 ± 0.03	0.10 ± 0.04	0.065 ± 0.016
R_a (μm)	Optical	$0.79 \pm 0.01^*$	0.93 ± 0.02	1.99 ± 0.01	4.05 ± 0.04
	Stylus	$0.42 \pm 0.01^*$	1.01 ± 0.03	2.1 ± 0.03	4.67 ± 0.28
	AFM	$0.042 \pm 0.009^*$	0.24 ± 0.02	0.071 ± 0.025	0.047 ± 0.012
Skewness	Optical	$-0.11 \pm 0.01^*$	-0.12 ± 0.02	-0.13 ± 0.02	-0.17 ± 0.02
	Stylus	0.04 ± 0.15	-0.05 ± 0.05	0.01 ± 0.05	-0.10 ± 0.09
	AFM	$0.25 \pm 0.25^*$	0.39 ± 0.17	1.56 ± 1.28	4.56 ± 3.6
Kurtosis	Optical	$2.72 \pm 0.04^*$	3.53 ± 0.12	3.54 ± 0.07	3.55 ± 0.14
	Stylus	2.48 ± 0.10	2.89 ± 0.09	3.24 ± 0.19	3.22 ± 0.22
	AFM	$3.02 \pm 0.33^*$	5.0 ± 0.7	22.9 ± 12.6	453 ± 388

presented in the previous section and applied to data sets obtained with optical and stylus profilometers. The values reported in table 2 are averaged over the number of available maps (see table 1 for number of scans), while the uncertainty indicates the mean deviation from the average value. The evolution of these statistical estimators with bead size is also reported in figure 3. The AFM data are purposely not reported here—the RMS roughness measured at sub micrometer scale is by definition smaller than that measured at micro-meter scale (as will be detailed in next section [?]). Figure 3(a) shows a striking dependence of the roughness fluctuations, here estimated by the RMS value σ on the size d of the beads used for the blasting process. As shown by the dashed line, the RMS data are consistent with an affine evolution of the RMS with the bead size, from 0.5 μm for the untreated samples to more than 5 μm for the sample blasted with the larger beads. This apparent additive evolution suggests that the surface roughness of the final blasted samples results from the superposition of the height fluctuations induced by the blasting process and of part of the height fluctuations of the initial un-treated surface. We thus get a clear impact of the size of beads

used during the blasting process, the increase of the beads size results in more profound impacts which sets the scale of the height fluctuations.

We note that only the value of the RMS of the initial sampled measured by optical profilometry does not follow this trend. This value actually grossly over-estimates the results obtained by stylus profilometry. The roughness level of the cold rolled surface about 500 nm is actually very close to the detection limit $\delta_h = 300$ nm of the optical profilometer. Moreover, the discrepancy in roughness measured with stylus profilometers and optical profilometers for sub-micrometer roughness have been already reported [63]. The height measurement obtained with the optical technique on the initial surface have thus to be taken with caution. They are labeled with a star in table 2.

As shown in figures 3(b) and (b), skewness and kurtosis values of the blasted samples slightly differ from the values expected for a normal distribution, $\gamma_3 = 0$ and $\gamma_4 = 3$, respectively. Unlike the evolution observed for the RMS roughness, neither the skewness nor the kurtosis show clear dependence on the bead size. We only observe a trend for negative skewness
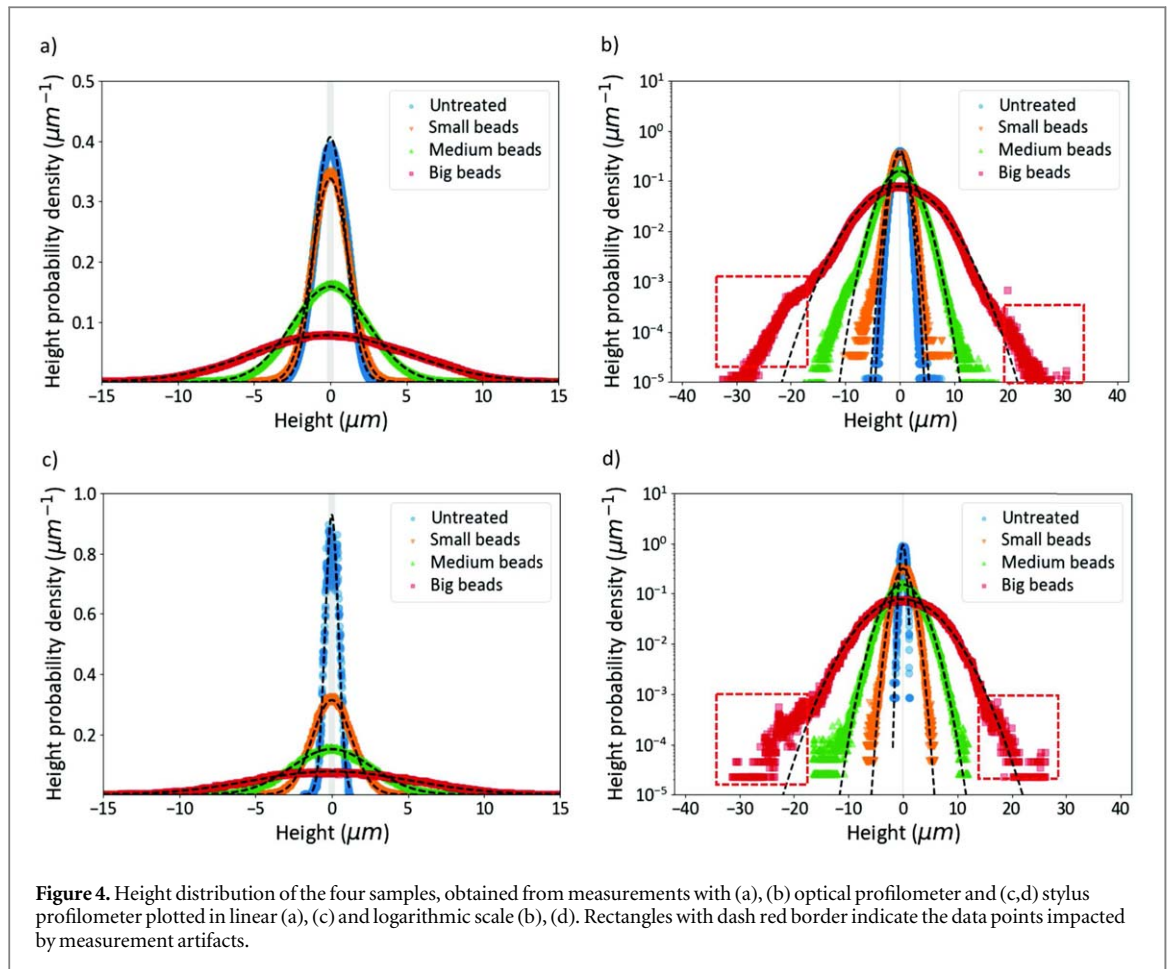
Figure 4. Height distribution of the four samples, obtained from measurements with (a), (b) optical profilometer and (c,d) stylus profilometer plotted in linear (a), (c) and logarithmic scale (b), (d). Rectangles with dash red border indicate the data points impacted by measurement artifacts.

and high kurtosis for the blasted samples in contrast to positive skewness /low kurtosis seen for the un-treated sample. Kurtosis 3 have already been reported for hard-turned surfaces [64], while slightly negative skewness and kurtosis 3are common for sand-blasted samples [28, 36]. The slight negative skewness observed for the blasted samples is a mark of the asymmetry of the surface and may reflect the presence of a superposition of craters, the positive kurtosis attests of a relative domination of the peak of the tails on the medium values of the distribution. These deviations to Gaussianity are however not spectacular and also appear to depend on the experimental technique of measurements.

It is thus of interest to give a closer look at the distributions of height fluctuations. In figures 4(a) and (c), we show the distributions obtained with the optical profilometer ans the stylus profilometer, respectively. Consistently with the RMS measurements reported in table 2 we observe that the blasting of the aluminum surface induces a clear bead size dependent broadening of the height distribution functions. Together with the measured height distributions, we also show Gaussian fits together with the measured distributions. An excellent agreement is observed.

In figures 4(b) and (d), the same data and Gaussian fits are plotted in semi-logarithmic scale. Small deviation from Gaussianity can now be identified in the tails

for the blasted samples. Interestingly we note that deviations appear to be more significant for the optical measurements than for the stylus measurements.

Before discussing more quantitative aspects, note that it is not that surprising that skewness and kurtosis are slightly dependent on the measurement techniques. Stylus profilometry relies on the contact between a smooth convex tip and the surface. The resulting height field can thus be seen as a kind of complex convolution of the surface with the tip shape with the very hard condition of non-penetrability. The latter constraint induces contrasting effects on peak and valleys and even surprising long-range correlations [65].

Yet, extremities of pdf tails are likely to be altered by measurement artifacts. No profilometer device allows for accurate measurement of steep walls or spikes, and the adjacent points can get artificially large or small values, which produces clearly non-Gaussian extremities of pdf in figures 4(a)–(b). In particular, the confocal optical profilometer has a limited accessibility range for the slopes, since the latter may not be independent of the heights, the exclusion of even a very small fraction of non-measurable points is susceptible to affect the estimates of high moments such as the skewness and the kurtosis.

To illustrate this point let us consider a distribution that perfectly follow the Gaussian expression (1) in the range $[-3\sigma, 3\sigma]$ and thus represent 99.73% of

the sampled values and let's complete it by one peak at 3σ that gathers the complementary 0.27% of the sampled values. the symmetric part gives a zero contribution to the skewness *s*. The latter is thus entirely controlled by the peak at $3\sigma : s = 0.027 \times 3^3 = 0.0729$. The same exercise can be performed for the kurtosis when we now consider that 99.73% of the sampled values are distributed according to a Gaussian distribution and that the remaining part is concentrated on two symmetric peaks at $\pm 3\sigma$. We get for the kurtosis $\kappa = 0.9973 \times 3 + 0.0027 \times 3^4 \approx 3.21$. Such values are not far from those estimated for our experimental data which are reasonably described by a Gaussian distribution in the range $[-3\sigma, 3\sigma]$.

4.3. Discussion on height distributions
In conclusion, for the examined blasted samples their height distribution and statistical parameters provide some differentiation between samples and some basic understanding of the impact of blasting on surface topography. But the way in which this asymmetry is induced by fabrication process remains to be captured.

Despite extensive measurements, the estimate of even the first higher moments remains fragile. In particular the dependence of kurtosis and skewness on the distribution tails makes them both statistically demanding and sensitive to instrumental artifacts. In the present case the crater-like morpology of the blasted surfaces suggests a negative skewness. Our measurements (see table 2) are indeed consistent with this expectation but the dependence of the results on the instrumental technique and the significant uncertainty forbid us to take this observation as a strong and robust result. Hence, it is of interest to perform complementary characterizations.

5. Spatial correlation

5.1. Theoretical context
The height distribution function of the surface provides information on the vertical fluctuation of the surface but it does not bring a full knowledge of the surface slopes. In the context of light scattering, the amplitude of the height fluctuations, typically specified by the ratio of the RMS roughness to the wavelength (σ/λ), controls the fraction of light scattered out of the specular direction but conveys no information about the angular range of the scattering [54]. The latter requires some knowledge of the spatial organization of the surface roughness.

In physics the classical tools used to access this information are in real space the surface height auto-covariance $\mathcal{I}(\Delta\mathbf{r})$ and its normalized version, the auto-correlation function $\mathcal{A}(\Delta\mathbf{r})$. In the Fourier space, the power spectrum density function $\widetilde{\mathcal{I}}(\mathbf{q})$ is the counterpart of the auto-covariance. Here the vector $\mathbf{q} = (q_x, q_y)$ represents the in-plane wave vector (which is parallel to the mean surface). Note that in

surface metrology the spatial correlations are evaluated through slightly different parameters—the fastest decay auto-correlation length (S_{al}) and texture aspect ratio of the surface (S_{tr}), density of summits S_{ds} etc. These parameters are used for the assessment of surface topography as for example described in [41]. But in this work we focus on surface estimators which can be used in physical models.

5.1.1. Auto-correlation function
The surface height auto-correlation function measures the resemblance of the height field to itself over a in-plane distance $\Delta r = |\Delta\mathbf{r}|$:

$$\mathcal{A}(\Delta\mathbf{r}) = \frac{\mathcal{I}(\Delta\mathbf{r})}{\mathcal{I}(\mathbf{0})} = \frac{1}{\sigma^2}\langle h(\mathbf{r} + \Delta\mathbf{r})h(\mathbf{r})\rangle. \quad (5)$$

The prefactor $1/\sigma^2$ ensures normalization: $\mathcal{A}(\mathbf{0}) = 1$ which also gives the maximum value of correlation. For randomly rough surface $\mathcal{A}(\Delta\mathbf{r}) < 1$ as soon as $|\Delta\mathbf{r}| > 0$ and $\mathcal{A}(\Delta\mathbf{r}) \rightarrow 0$ when $|\Delta\mathbf{r}| \rightarrow \infty$. In the case of an isotropic surface, the function $\mathcal{A}(\Delta\mathbf{r})$ depends on $\Delta\mathbf{r}$ only through it length $\Delta r = |\Delta\mathbf{r}|$ and not on its direction. In such cases it is customary to define a correlation length ℓ_c that estimates the (lateral) length scale above which correlation is significant. Developed for the exponential and Gaussian forms of the auto-correlation function, a typical definition consists of taking the length for which the auto-correlation function has dropped to $1/e$ (from its value of one at $\Delta\mathbf{r} = 0$):

$$\mathcal{A}(\ell_c) = \frac{1}{e}. \quad (6)$$

This conventional definition of the correlation length ℓ_c implicitly assumes a Gaussian or exponential form of the auto-correlation function. Although these forms of the auto-correlation function are the most commonly used in theoretical description of randomly rough surfaces, they do not exhaust the variety of the functional forms (Lorentzian, Bessel, etc.) which can be encountered on real rough surfaces [39]. Note that in metrological definition of the auto-correlation length Sal may differ from the physical definition of correlation length. In metrology, Sal is defined from 3D surface scan as the fastest decay reaching a given value—often 0.2 [66] or $1/e$ [67].

In particular, a rough surface can be characterized by several length scales. A microscopic length scale associated with the structure of the material can coexist with a larger length scale associated with a forming process, etc. An example is given by the correlation of mounded surfaces which combine a fast decay with an oscillatory behavior. The auto-correlation function of such surfaces is typically written as follows [39, 68]:

$$\mathcal{A}(\Delta r) = \exp\left[-\left(\frac{\Delta r}{\ell_0}\right)^{2\alpha}\right]\cos\left(\frac{2\pi\Delta r}{\Lambda}\right), \quad (7)$$

where α denotes the roughness exponent which usually takes a value between 0 and 1 $(0 \leqslant \alpha \leqslant 1)$. While the decay can be described by a stretched or a

compressed exponential, we see that two characteristic length scales emerge from this definition. The first one, ℓ_0 is associated with the fast decay and gives an estimate of the size of the mounds. The second length scale, Λ gives the period of the attenuated oscillations and is related to the average distance between mounds. In the case of mounded surfaces, the correlation length scale ℓ_c as conventionally defined in equation (6) depends jointly on ℓ_0 and Λ.

More generally, the above definition of ℓ_c does not ensure the absence of correlations for lags beyond ℓ_c. In the example of mounded surfaces, due to the exponential form of the decay, the correlations are short-ranged. In theory, height correlations may be characterized by a multiplicity of length scales. An interesting limit is obtained in the case of power-law correlations which can also be considered as a continuum of characteristic length scales. This case of *long-ranged* height correlations corresponds to self-affine surfaces [39, 69–71]. Such surfaces have the particular property to remain statistically invariant by the family of anisotropic transformations: $\mathbf{r} \to \lambda \mathbf{r}$, $z \to \lambda^H z$ where λ is a positive real scaling factor and H an exponent usually in the range [0, 1]. In the case of long-range correlations, it is usually more convenient to work with the statistics of height increments rather than with the classical auto-correlation function. In particular, the self-affine invariance induces a power law scaling of the second moment of the height increments [71]:

$$\langle |h(\mathbf{r} + \Delta\mathbf{r}) - h(\mathbf{r})|^2 \rangle = \ell_0^{2(1-H)} \Delta r^{2H}. \quad (8)$$

Here the length scale ℓ_0 sets the amplitude of the height fluctuations. This length scale, also known as the *topothesy*, is defined so that the average slope measured over a distance ℓ_0 is of the order unity. Note that the scaling behavior usually only holds within a finite range of length scales $\ell_{\min} < \Delta r < \ell_{\max}$. When the macroscopic length of measurements L lies within this range, this means, in particular, that the experimental RMS roughness becomes length scale dependent [71]:

$$\sigma(L) \propto \ell_0^{1-H} L^H. \quad (9)$$

The surfaces obtained through mechanical interaction between solids are expected to have fractal properties with $H = 0.85 \pm 0.15$ [72]. In the above definitions, the rough surface was considered to be isotropic. In the case of anisotropic surfaces, it is generally possible to distinguish two principal directions which can be characterized by different correlation lengths (for short-ranged correlations) or self-affine parameters (for long-ranged correlations).

5.1.2. Power spectral density

The surface height auto-correlation function provides a rather intuitive insight into over which regions the surface heights are correlated. Many physical models rather rely on its counterpart in the Fourier space, namely the *power spectrum* of the surface roughness,

$\widetilde{\mathcal{I}}(\mathbf{q})$, also known as the power spectral density (PSD). For example, in mechanics the PSD is used to characterize adhesion, true contact area, or contact stiffness [60], while in optics of very weakly rough surface the diffusely scattered light is proportional to the PSD [12, 54, 59]. The PSD is related to the surface height auto-covariance function by a Fourier transform (a direct consequence of the Wiener-Khinchin theorem [73]):

$$\widetilde{\mathcal{I}}(\mathbf{q}) = \int d^2r \, \mathcal{I}(\mathbf{r}) \exp(-i\mathbf{q} \cdot \mathbf{r}), \quad (10)$$

and from the inverse Fourier transform it follows that the auto-correlation $\mathcal{A}(\mathbf{r}) = \mathcal{I}(\mathbf{r})/\sigma^2$ can be expressed as:

$$\mathcal{A}(\mathbf{r}) = \frac{1}{\sigma^2} \int \frac{d^2q}{(2\pi)^2} \widetilde{\mathcal{I}}(\mathbf{q}) \exp(i\mathbf{q} \cdot \mathbf{r}). \quad (11)$$

In terms of the Fourier transform of the surface roughness

$$\widetilde{h}(\mathbf{q}) = \int d^2r \, h(\mathbf{r}) \exp(-i\mathbf{q} \cdot \mathbf{r}), \quad (12)$$

the power spectrum of the surface roughness, can equivalently be defined as [10]:

$$\widetilde{\mathcal{I}}(\mathbf{q}) = \frac{\langle |\widetilde{h}(\mathbf{q})|^2 \rangle}{S}, \quad (13)$$

where S is the area of the mean surface covered by the random surface. The latter form of $\widetilde{\mathcal{I}}(\mathbf{q})$ (equation (13)) does not require one to first calculate the correlation function. Due to this practical convenience, equation (13) is preferred over the form in equation (10) while dealing with experimental data. Moreover, it is of a common practice to first calculate the power spectrum via equation (13) and then to use this result in equation (11) to obtain $A(\mathbf{r})$.

Yet, contrary to the ACF, some care has to be taken while comparing PSD of surface morphology measured over an area (two-dimensional scan) or a line (one-dimensional scan) of the mean plane [4, 74]. From Parseval's theorem [12] the integral of the PSD equals the variance of the height distribution (σ^2) leading to different normalization for the PSD obtained from one-dimensional and two-dimensional scans, referred here-after as 1D-PSD and 2D-PSD respectively:

$$\int \frac{dq_x}{2\pi} \widetilde{\mathcal{I}}_{1D}(q_x) = \sigma^2; \qquad \int \frac{d^2q}{(2\pi)^2} \widetilde{\mathcal{I}}_{2D}(\mathbf{q}) = \sigma^2, \quad (14)$$

where for the sake of simplicity, the line is assumed to be oriented along the *x*-axis, and the corresponding line-scans, or one-dimensional surface profiles, are denoted $h(x, 0)$. Note that 1D and 2D-PSD have different units, namely m^3 and m^4, respectively.

In the special case of an isotropic surface it can be demonstrated that the one-dimensional power spectrum of the surface profile, $\widetilde{\mathcal{I}}_{1D}(q_x)$, is related to the power spectrum of the two-dimensional surface profile $\widetilde{\mathcal{I}}_{2D}(|\mathbf{q}|)$ by the relation [4, 48]:
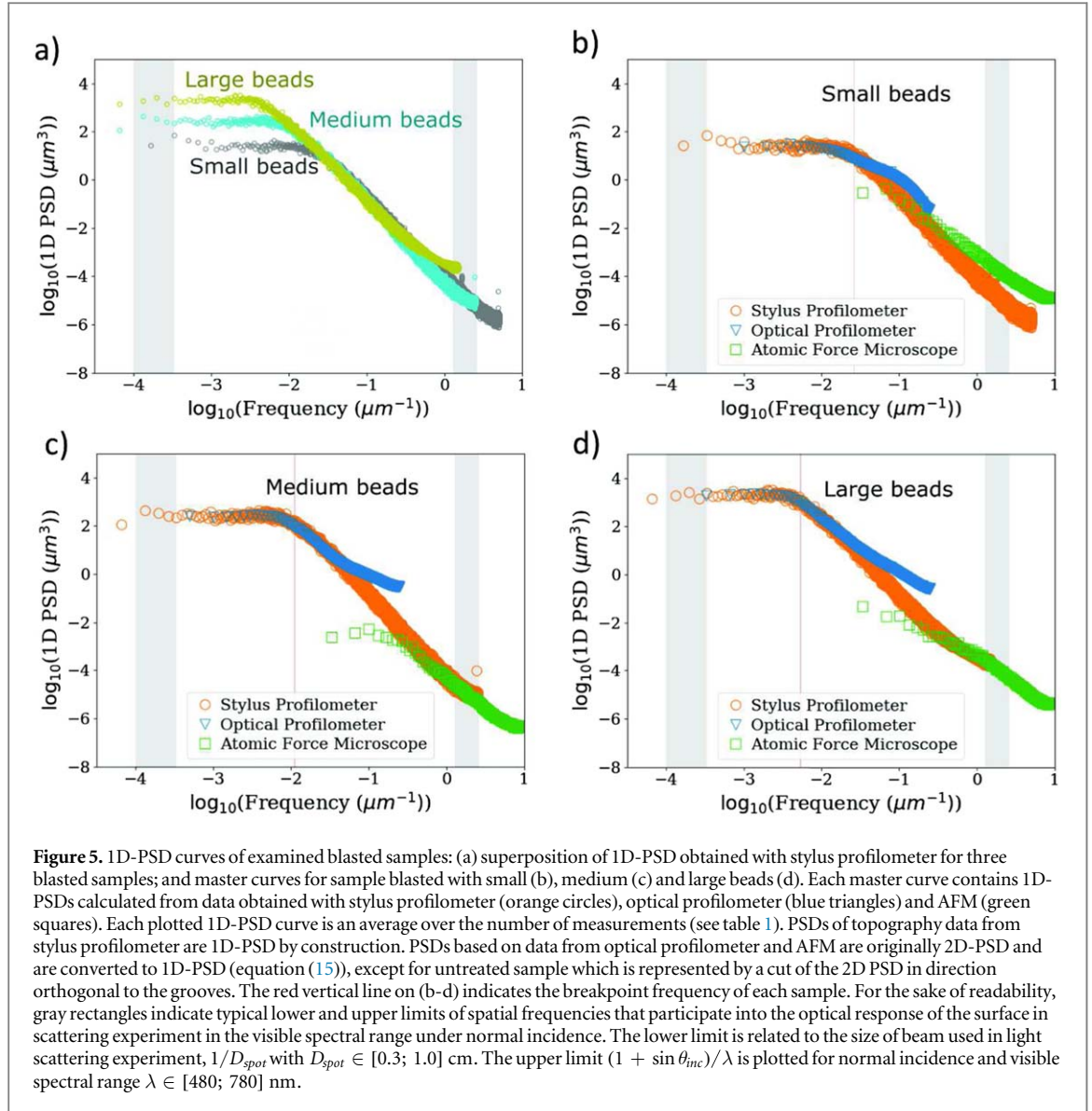
Figure 5. 1D-PSD curves of examined blasted samples: (a) superposition of 1D-PSD obtained with stylus profilometer for three blasted samples; and master curves for sample blasted with small (b), medium (c) and large beads (d). Each master curve contains 1D-PSDs calculated from data obtained with stylus profilometer (orange circles), optical profilometer (blue triangles) and AFM (green squares). Each plotted 1D-PSD curve is an average over the number of measurements (see table 1). PSDs of topography data from stylus profilometer are 1D-PSD by construction. PSDs based on data from optical profilometer and AFM are originally 2D-PSD and are converted to 1D-PSD (equation (15)), except for untreated sample which is represented by a cut of the 2D PSD in direction orthogonal to the grooves. The red vertical line on (b-d) indicates the breakpoint frequency of each sample. For the sake of readability, gray rectangles indicate typical lower and upper limits of spatial frequencies that participate into the optical response of the surface in scattering experiment in the visible spectral range under normal incidence. The lower limit is related to the size of beam used in light scattering experiment, $1/D_{spot}$ with $D_{spot} \in [0.3; 1.0]$ cm. The upper limit $(1 + \sin \theta_{inc})/\lambda$ is plotted for normal incidence and visible spectral range $\lambda \in [480; 780]$ nm.

$$\widetilde{\mathcal{I}}_{1D}(q_x) = \frac{1}{\pi} \int_0^\infty dq_y \widetilde{\mathcal{I}}_{2D}(|\mathbf{q}|), \qquad (15)$$

where $|\mathbf{q}| = \sqrt{q_x^2 + q_y^2}$ and $q_x, q_y \geqslant 0$.

In the case of self-affine surfaces the 1D-PSD follows the scaling relation [39]:

$$\widetilde{\mathcal{I}}_{1D}(q_{x,y}) \propto \ell_0^{2(1-H_{x,y})} q_{x,y}^{-1-2H_{x,y}},$$
$$\frac{2\pi}{\ell_{\max}} < q_{x,y} < \frac{2\pi}{\ell_{\min}} \qquad (16)$$

where we considered an anisotropic surface with two different roughness exponents H_x and H_y along the x-axis and the y-axis respectively.

In the case of mounded surfaces with roughness exponent $\alpha = 1$ [39]:

$$\widetilde{\mathcal{I}}_{1D}(q_x) = \frac{\sigma^2 \ell_c}{2\sqrt{2}} \left[e^{-\left(q_x - \frac{2\pi}{\lambda}\right)^2 \frac{\ell_c^2}{4}} + e^{-\left(q_x + \frac{2\pi}{\lambda}\right)^2 \frac{\ell_c^2}{4}} \right], \quad (17)$$

In practice, power spectrum densities often exhibit distributions close to that of a low-pass filter [4]. Interestingly, the spatial frequency of the breakpoint q_B between the constant low-frequency part and the

decaying high-frequency part is related to the correlation length. For instance, in surfaces with exponential ACF, $q_B = 1/(2\pi\ell_c)$.

In summary, while dealing with experimental surface profile data, the power spectrum density is evaluated on the basis of equation (13), but direct comparison of the PSD obtained from one-dimensional and two-dimensional data is delicate due to the difference in normalization of the PSD. Therefore, in order to make the PSD master-curve combining data from different setups for height measurements, the PSD curves must be brought to one-dimensional or two-dimensional case. In this work, one-dimensional PSDs were chosen as the master curves.

5.2. Experimental results

5.2.1. Power spectral density

The 1D-PSD master curves [9, 74] for the three blasted samples are shown in figure 5. Figure 5(a) shows a superposition of the PSDs obtained with stylus profilometry for the three blasted samples. The

construction of 1D-PSD master curve from data measured with different techniques is illustrated in figures 5(b)–(d) for blasted samples. The 1D-PSD were directly obtained from one dimensional profiles, measured with stylus profilometer. Meanwhile, 2D-PSD were calculated based on 2D topography data from optical profilometer and AFM. Since the blasted samples had isotropic 2D-PSDs, the latter were converted to 1D-PSDs according to equation (15). The results shown in figures 5(b)–(d) illustrate the interest and the difficulty of the present multiscale characterization. With the three experimental techniques used in thus study (optical profilometry, stylus profilometry, AFM), the measurements span 5 orders of magnitude for the spatial frequencies. This allows us to access contrasting correlation regimes and to give a full characterization of the surface roughness. While the consistency of the different measurement techniques is overall very good, some discrepancies can be observed, especially at the bounds of the range of accessible spatial frequencies of each technique. High frequencies are sensitive to the nature of the local probe (mechanical tip vs optical probe) while low frequencies typically suffer from a relative lack of statistics. Beyond these classical issues we remark that the collapse between the different measurements for the surface blasted with small beads is of lesser quality than for those blasted with medium and large beads. This raises the question of statistical representativity of small scale measurements (her AFM) when compared to large scale measurements and more generally the effective stationarity of the height fluctuations over the surface.

In light scattering experiments within the visible spectral range the spatial frequencies of the surface roughness higher than $(1 + \sin\theta_{inc})/\lambda$ (where θ_{inc} is the angle of incidence of the incoming light of wavelength λ) do not participate in the optical response [22]. This upper spatial frequency limit is presented in figure 5 for the visible spectral range ($\lambda \in [480, 780]$ nm) in the case of normal incidence by a gray rectangle on the right side of each figure. Meanwhile, the size D_{spot} of the illumination spot used in the optical experiment defines the lowest limit $1/D_{spot}$ of spatial frequencies that contribute to the optical response [22]. This lower spatial frequency limit is indicated in figure 5 by a gray rectangle on the left side of each figure for $D_{spot} \in [0.3, 1.0]$ cm, order of magnitude of spot size generally used in angle resolved light scattering experiments.

Blasted samples exhibit a constant PSD of value $\widetilde{\mathcal{I}}_0$ at low spatial frequencies and a decay of PSD for higher spatial frequencies. The breakpoint between these two regimes provides for each sample a characteristic spatial frequency, referred hereafter as breakpoint spatial frequency q_b, at which the PSD values is decreased by a factor of 2 as compared to the constant low-frequency value $\widetilde{\mathcal{I}}_{1D}(q_b) = \widetilde{\mathcal{I}}_0/2$ [4]. In examined samples $(\widetilde{\mathcal{I}}_0, q_b/(2\pi)) = (25\ \mu\mathrm{m}^3, 0.026\ \mu\mathrm{m}^{-1})$ for samples blasted with small beads, $(251\ \mu\mathrm{m}^3, 0.011\ \mu\mathrm{m}^{-1})$ and $(1995\ \mu\mathrm{m}^3, 0.0053\ \mu\mathrm{m}^{-1})$ for samples blasted with medium and large beads respectively. Interestingly, the inverse of the breakpoint spatial frequencies match rather well with the average radius of the beads used during the blasting: $(2\pi/q_b, \mathrm{d}) = (38\ \mu\mathrm{m}, 35\ \mu\mathrm{m})$ for samples blasted with small beads, $(89\ \mu\mathrm{m}, 100\ \mu\mathrm{m})$ and $(186\ \mu\mathrm{m}, 250\ \mu\mathrm{m})$ for samples blasted with medium and large beads respectively.
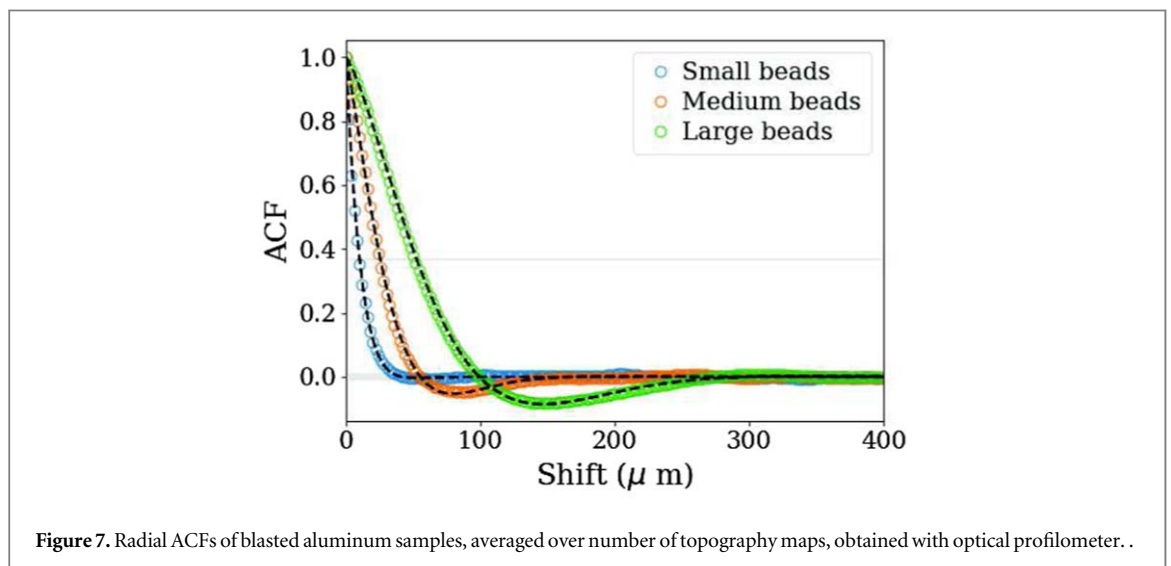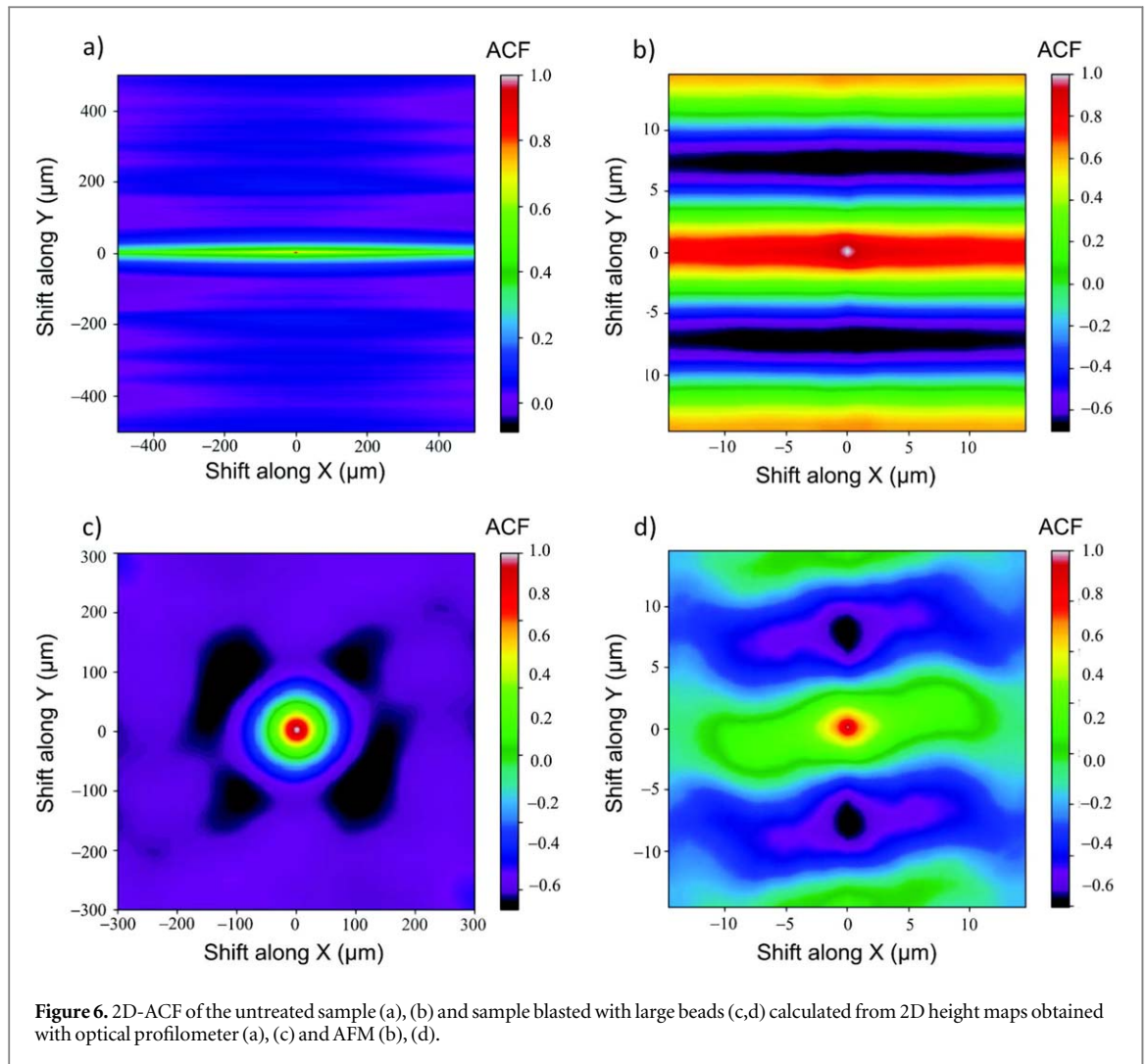
In conclusion, in the case of blasted metallic surfaces, characteristic features of the PSD happen to appear exactly within the spatial frequency range, which features their optical response. Moreover, there seems to be a direct link between the features in the PSD and the parameters of fabrication process. While the low spatial frequency part of the PSDs strongly depends on the bead size, we note that the 3 PSDs collapse on the same power-law like behavior in the high spatial frequency regions. This suggests that the high-frequency roughness either stems from the untreated surface or from the micro-roughness of the beads.

5.2.2. Auto-correlation function

Figures 6(a) and (b) show the 2D anisotropic auto-correlation functions of the untreated sample calculated from the height maps obtained with the optical profilometer (figure 6(a)) and the AFM (figure 6(b)). Both figures show a striking anisotropy. Here the ACF along the *x* axis (along the grooves) is slowly decaying in both graphs, while the ACF along the *y* axis (orthogonal to the grooves) exhibits a steeper decay and a bump in both graphs.

The ACF along the *y* axis in figure 6(a) is characterized by $\ell_c = 3.0 \pm 0.05\ \mu\mathrm{m}$ and has a peak at $\ell_p = 10.0 \pm 0.5\ \mu\mathrm{m}$, which corresponds to the average distance between the groves. Meanwhile, the fine-resolution measurements with AFM allow to observe $\ell_c = 1.8 \pm 0.6\ \mu\mathrm{m}$ and the anti-correlation features at $5.1 \pm 2.4\ \mu\mathrm{m}$, which corresponds to half a distance between the grooves. The incertitude indicates the standard deviation over the measurements. The measurement step of the optical profilometer and stylus profilometer are too large to resolve this anti-correlation.

We will now analyze the ACF of the blasted samples, starting with the large-scale measurements, namely data obtained with the optical profilometer, and then focusing on the data obtained at small-scale (AFM). For all the blasted samples the 2D ACF obtained from the optical profilometer exhibit radial symmetry for spatial frequencies within the correlation length, as illustrated by figure 6(c) for sample blasted with large beads. The radial average of these 2D ACFs are presented in figure 7. None of them follow exponential or Gaussian forms The correlation lengths ℓ_c were estimated from the conventional definition

Figure 6. 2D-ACF of the untreated sample (a), (b) and sample blasted with large beads (c,d) calculated from 2D height maps obtained with optical profilometer (a), (c) and AFM (b), (d).

Figure 7. Radial ACFs of blasted aluminum samples, averaged over number of topography maps, obtained with optical profilometer. .

given by equation (6) and the results are summarized in table 4. In fact, for all three samples the ACF exhibits anti-correlation features, which are seen as local negative-valued minimum of the ACFs, referred hereafter as ℓ_{ac}. For measurements with the optical profilometer, it appears at approximately 42.9 μm, 78.2 μm

and 146.2 μm for small, medium and large beads, respectively. Interestingly, for data obtained with the optical profilometer all three blasted samples $\ell_{ac}/\ell_c \cong 3$. Contact profilometer provides similar values, but the authors find averaging over 2D profiles more accurate and thereby rely hereafter on the data

obtained with the optical profilometer for the analysis of the ACF.

Meanwhile, data obtained with the AFM (figures 6(b) and 6(d) for the untreated sample and the sample blasted with large beads, respectively) suggest that the surface profiles of all four samples exhibit anisotropic anti-correlation behavior at length scale of the order of 10 μm: about 7 μm for the untreated sample and the samples blasted with small and medium beads, a slightly larger value for sample blasted with large beads. Thereby the blasting process induces a 50–100 μm scale micropattern on the surface of the aluminum plates, but it fails to completely erase the anisotropic 10 μm scale pattern induced by the rolling process during the fabrication of bare aluminum plates.

The empirical ACFs were fitted with the functional form given by equation (7). In this way one obtained the values $(\ell_0, \Lambda, \alpha) = (11\ \mu\text{m}, 166\ \mu\text{m}, 0.50)$ for samples blasted with small beads; $(35\ \mu\text{m}, 222\ \mu\text{m}, 0.55)$ for samples blasted with medium beads; and finally $(80\ \mu\text{m}, 397\ \mu\text{m}, 0.60)$ for samples blasted with large beads (table 4).

The correlation length ℓ_c and anti-correlation length ℓ_{ac} vary linearly with the average bead size, same does the RMS value. The ratio RMS to ℓ_c is however constant with bead size and one would expect similar slope distributions. Yet, due to the difference in the shape of impacts and as will be shown in section 6, the distributions of slope angles of these samples are not the same. Conventional definition of ℓ_c (see equation (6)) may seem less convincing in the case of surfaces with non-exponential and non-Gaussian ACFs. Yet, for all examined blasted samples $2\pi/q_b \cong 3.7\ell_c$, while in surfaces with exponential auto-corellation function $2\pi/q_b \cong 2\pi\ell_c$. In order to avoid errors in the interpretation, both ℓ_c and q_b should be analyzed.

5.3. Discussion on height correlations

In contrast to the height distribution, which often is found to be Gaussian, the surface height correlation function shows a wide variety in the functional form that it exhibits. Moreover, rough surfaces can exhibit multiscale correlations. For example, the blasted samples examined in this work the multiscale correlation is evident from the two following features: (i) the emergence of a characteristic length associated to the impact of the blasting beads (as shown by figure 7 and the optical and stylus profilometer data in table 3) and (ii) the persisting long-range correlation in the high-frequency tail (figure 5 and AFM data in table 3), possibly originating from the self-affine character of the initial surfaces before blasting.

In particular, as shown in figure 8(a), we observe that large scale measurements show the existence of two characteristic length scales (correlation and anti-correlation) that grow linearly with the bead size. Still,

as suggested by the collapse of the high frequency parts of the PSDs (Figure 5) and the persistence of anisotropic patterns in the ACFs obtained by AFM on blasted samples (figure 7) the microscale roughness as measured by AFM shows a contrasting trend. As shown in figure 8(b), in this range of small lateral scales, the correlation length ℓ_c^{AFM} and the anti-correlation length ℓ_{ac}^{AFM} appear to stay unaffected by the blasting process.

6. Surface slopes

In some cases it is more convenient to characterize the surface roughness through the slopes rather than the heights, as for example in geometrical optics and mechanics [49]. Indeed, the microfacet theory [14–16] on which the computer graphics is based, represents a rough surface as a collection of planar facets. The size of an individual facet is assumed to be larger than the wavelength of the incident light so that the geometrical optics description can be applied. The macrosurface is assumed to be flat on average, and the orientation of the mean surface in space is defined by the unit normal vector $\mathbf{n} = (0, 0, 1)$, which points from the surface towards the ambient medium. The orientation of a single microfacet is described through a unit normal vector $\mathbf{m}$, while its angle θ_m with respect to $\mathbf{n}$ can be rather large. In optical models based on the microfacet theory, light scattering from rough surfaces is strongly dependent on the statistics assumed for the orientation of individual facets, referred to as *microfacet distribution* $p(\theta_m)$.

6.1. Theoretical context

The knowledge of surface slopes is thus of primary interest for the determination of the optical properties of the surface. However, their determination, *a priori* immediate from the knowledge of height profiles is more subtle than is commonly believed. The definition of local slopes in a physical context usually suffers from ambiguity. Mathematically the slopes of the surface are easily defined through the height gradients provided that the height profile respects the required conditions of regularity. Many different algorithms have been developed for estimating the slope of a surface from experimental topography data sets [75]. Those algorithms involve slope definition on different amount of points. However, in a physical context, local slopes should be defined over a typical length scale. To give a simple example, the angular width of the light reflected by a moderately rough surface is controlled by the average slope $s(\ell)$ estimated over a lateral length scale of $\ell \sim \lambda$ [45, 54, 71]. Such local slopes depend on the length scale over which they are defined. For instance, consider rough surfaces characterized by a correlation length ℓ_c. One naturally expects the slopes $s(\ell)$ to reach a maximum for $\ell < \ell_c$ and to vanish for $\ell \gg \ell_c$. Moreover as will be

Table 3. Correlation length ℓ_c and anti-correlation length ℓ_{ac} parameters extracted from experimental characterization of blasted aluminum plates and reference untreated plate. In case of measurements of untreated sample and AFM measurements of all samples the provided values of ℓ_c and ℓ_{ac} correspond to the measurement direction perpendicular to the grooves. In case of measurements with optical profilometer ℓ_c and ℓ_{ac} were calculated from radial average of 2D ACF maps, while in case of measurements with stylus profilometer as average over 1D ACFs obtained from measurements along x and y directions.

Estimator	Setup	Untreated sample	Small beads	Medium beads	Large beads
ℓ_c (μm)	Optical profilometer	1.8 ± 0.6	9.0 ± 0.3	25.6 ± 0.3	50.0 ± 0.7
	Stylus profilometer	13.4 ± 0.7	10.9 ± 0.5	24.7 ± 0.5	47.3 ± 3.1
	AFM	1.6 ± 0.1	2.2 ± 1.1	1.1 ± 0.5	2.2 ± 1.1
ℓ_{ac} (μm)	Optical profilometer	—	42.9 ± 3.8	78.2 ± 2.4	146.2 ± 4.5
	Stylus profilometer	—	35.6 ± 10.9	76.0 ± 12.0	145 ± 18.4
	AFM	5.1 ± 2.4	7.0 ± 3.5	5.8 ± 2.9	7.8 ± 3.9

discussed below, this size-dependence of the local slopes is also impacted by the nature of the form of the height auto-correlation function. For a given form of the correlation function, one can calculate the form of $s(\ell)$ as will be shown in the following.

6.1.1. From height correlation to slope distribution

The sum or difference of two Gaussianly distributed random variables is itself a random Guassian variable. In the case of a Gaussian height distribution, we can thus define the height difference $\Delta h(\Delta \mathbf{r}) = h(\mathbf{r} + \Delta \mathbf{r}) - h(\mathbf{r})$ over $\Delta \mathbf{r}$ as a random Gaussian variable. The variance $\langle |\Delta_r h|^2 \rangle$ naturally depends on the distance $\Delta r = |\Delta \mathbf{r}|$ through the height autocorrelation function $\mathcal{A}(\Delta \mathbf{r})$. In the case of isotropic short-range correlations, we thus get:

$$\langle |\Delta h|^2 \rangle (\Delta r) = 2\sigma^2 [1 - \mathcal{A}(\Delta r)]. \quad (18)$$

In one dimension, the local slopes s_ℓ over the length scale ℓ are thus immediately defined as:

$$s_\ell = \left\langle \frac{h(\mathbf{r} + \Delta \mathbf{r}) - h(\mathbf{r})}{\Delta r} \right\rangle_{\mathbf{r}; |\Delta \mathbf{r}| = \ell},$$

where we average over $\mathbf{r}$ and the orientation of $\Delta \mathbf{r}$. If the height distribution is Gaussian, we get immediately for the slope distribution:

$$p(s_\ell) = \frac{1}{\sigma_{s,\ell} \sqrt{\pi}} \exp\left(-\frac{s_\ell^2}{2\sigma_{s,\ell}^2} \right), \quad (19)$$

where the standard deviation of local slopes is given by:

$$\sigma_{s,\ell} = \sqrt{2} \frac{\sigma}{\ell} \sqrt{1 - \mathcal{A}(\ell)}. \quad (20)$$

The knowledge of the height auto-correlation $\mathcal{A}$ thus gives us access to the statistics of the local slopes and the behaviour of $\sigma_{s,\ell}$ when $\ell \to 0$. We illustrate below the effect of the nature of the correlation on the standard deviation $\sigma_{s,\ell}$ of the local slopes and present them in figure 9:

- Gaussian correlation—If the length scale ℓ is small with respect to the correlation length ℓ_c ($\ell \ll \ell_c$), a simple Taylor expansion of the exponential

function can be used to get:

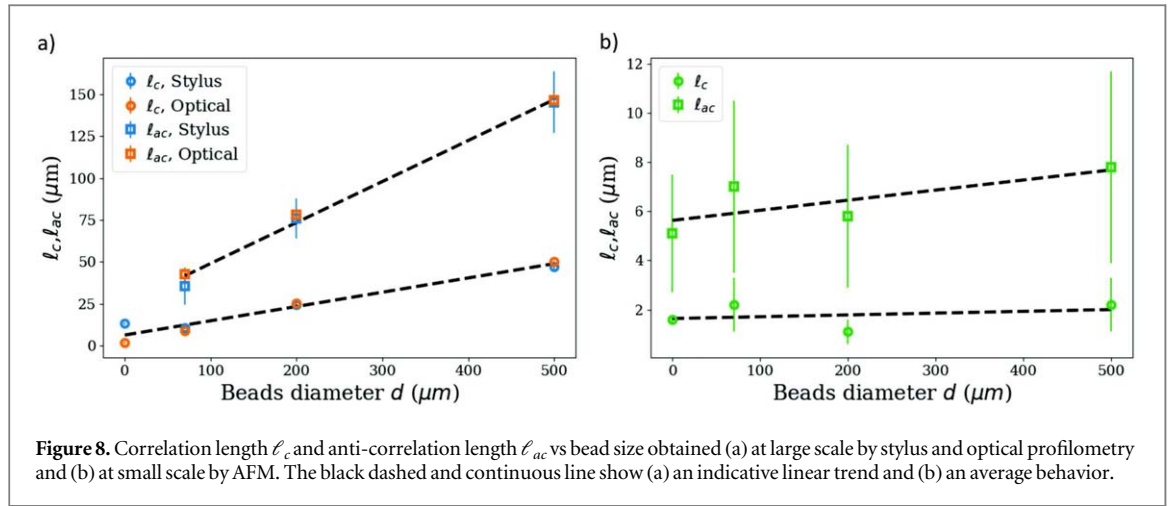$$\sigma_{s,\ell}^G = \sqrt{2} \frac{\sigma}{\ell} \sqrt{1 - \exp(-\ell^2/\ell_c^2)} \approx \sqrt{2} \frac{\sigma}{\ell_c}. \quad (21)$$

We note that this value is independent of ℓ: sufficiently well below the correlation length ℓ_c the statistics of local slopes do not depend on the length scale ℓ over which the slope is estimated. As depicted on figure 9(a), the statistics of the local slopes can be defined at a length scales $\ell < \ell_c/5$. In particular the variance σ'_s of the height gradients (corresponding to the limit of vanishing ℓ) should give the very same result $\sigma_s'^G = \sqrt{2} \sigma/\ell_c$.

- Exponential correlation—In this case, the Taylor expansion valid for $\ell \ll \ell_c$ gives:

$$\sigma_{s,\ell}^E = \sqrt{2} \frac{\sigma}{\ell} \sqrt{1 - \exp(-\ell/\ell_c)} \approx \sigma_{s,\ell}^G \sqrt{\ell_c/\ell} \quad (22)$$

Here the standard deviation of local slopes $\sigma_{s,\ell}$ shows a strong dependence on the length scale ℓ and is even expected to diverge in the limit of vanishing ℓ; This is seen in figure 9(a). Strictly speaking the standard deviation σ'_s of height gradients is thus no longer defined in the case of exponential correlation. In practice we expect the latter to be controlled by a cut-off scale $\ell_{\min}$, either defined as the scale below which the height correlation recovers a more regular Gaussian-like behavior or as a lower cut-off imposed by the instrument (tip diameter, optical wavelength) or by the sampling. The divergent behavior of the typical slope highlights the need to precise the length scale over which slopes are computed.

- The ACF of mounded surfaces— This particular class of surfaces has two characteristic length scales. They are the parameter ℓ_0, which defines how the correlation function decays (see equation (7)), and the average distance between mounds Λ, where $\ell_0 < \Lambda$. Here we will focus on the ACF exhibited by the blasted samples studied in subsequent sections and which form is given by equation (7), with in our case $\ell_c < \ell_0 \cong 0.42\ell_{ac} < \Lambda$. The standard deviation

Figure 8. Correlation length ℓ_c and anti-correlation length ℓ_{ac} vs bead size obtained (a) at large scale by stylus and optical profilometry and (b) at small scale by AFM. The black dashed and continuous line show (a) an indicative linear trend and (b) an average behavior.

of the local slopes in this case is:

$$\sigma_{s,\ell}^M = \sqrt{2}\frac{\sigma}{\ell}\sqrt{1 - \exp\left[-\left(\frac{\ell}{\ell_0}\right)^{2\alpha}\right]\cos\left(\frac{2\pi\ell}{\Lambda}\right)}. \tag{23}$$

As depicted in figure 9(a) the case $\alpha = 1$ is similar to the Gaussian ACF. For $\ell < \ell_c/10$ the standard deviation of the local slopes does not depend on the length scale over which slopes are computed, but the value is larger compared to the case of the Gaussian ACF. If $\alpha \leqslant 0.5$, the slope distribution is very similar to the one of exponential ACF and standard deviation of local slopes strongly depends on the length scale.

- Self-affine correlation—This dependence on length scales is even more pronounced in the case of self-affine surfaces. Here we have $\langle|\Delta h|^2\rangle(\ell) = \ell_0^{2-2H}\ell^{2H}$ where the length scale ℓ_0 is an amplitude parameter and H the roughness or Hurst exponent usually lying in the range [0, 1] [76]. Such a power-law behavior is usually only observed in a finite range of length scales [$\ell_{min} - \ell_{max}$]. In the case of self-affine height correlation, we thus get for the standard deviation of the local slopes [71]:

$$\sigma_{s,\ell}^{SA} = \left(\frac{\ell}{\ell_0}\right)^{H-1}. \tag{24}$$

Here again, the typical slope $\sigma_{s,\ell}$ strongly depends on the length scale ℓ over which it is estimated and the height gradient is ill-defined, as shown on figure 9(b). We note that the maximum slope is controlled by the lower cut-off ℓ_{min} of the self-affine regime $s_{max} \approx (\ell_{min}/\ell_0)^{H-1}$ while the RMS roughness $\Sigma = \ell_0^{1-H}\ell_{max}^H$ is controlled by the upper cut-off ℓ_{max} [71].

6.1.2. Facets and two-dimensional slope distribution
The probability density distribution of slopes in case of a 2D surface profile is as follows:

$$p_{2D}(s_{\ell_x}, s_{\ell_y}) = \frac{1}{2\pi\sigma_{s,\ell_x}\sigma_{s,\ell_y}}\exp\left\{-\frac{1}{2}\left[\left(\frac{s_{\ell_x}}{\sigma_{s,\ell_x}}\right)^2 + \left(\frac{s_{\ell_y}}{\sigma_{s,\ell_y}}\right)^2\right]\right\}, \tag{25}$$

For an isotropic surface, the variance of the slope distribution is independent on the axis along which it is estimated, or $\sigma_{s,\ell} = \sigma_{s,\ell_x} = \sigma_{s,\ell_y}$ as soon as the slopes are estimated over the same length scale $\ell = \ell_x = \ell_y$.

If we consider a facet defined by its extent ℓ (the projected distance over the mean plane) and its normal $\mathbf{n} = (\sin\theta_m\cos\varphi, \sin\theta_m\sin\varphi, \cos\theta_m)$, the slopes which can be estimated over the facet obviously depend on the direction. In particular, since slopes are defined here with respect to the horizontal plane, the angle ϕ gives the direction of the maximum slope $s_{m,\ell}$ while the slope vanishes along the orthogonal direction ($\varphi + \pi/2$). In particular we have:

$$s_{m,\ell} = \tan\theta_m = \sqrt{s_{\ell,x}^2 + s_{\ell,y}^2}. \tag{26}$$

The maximum slope $s_{m,\ell}$ acts here as a norm of the local slope vector (s_{ℓ_x}, s_{ℓ_y}) and is a positive quantity. Since the two variables s_{ℓ_x} and s_{ℓ_y} are Gaussian, the statistics of $s_{m,\ell}$ follows the χ-distribution:

$$p(s_{m,\ell}) = \frac{s_{m,\ell}}{\sigma_{s,\ell}^2}\exp\left(-\frac{s_{m,\ell}^2}{2\sigma_{s,\ell}^2}\right) \tag{27}$$

whose mode is located at $s_{m,\ell} = \sigma_{s,\ell}$. The maximum of the χ-distribution thus directly gives access to the standard deviation of the local slopes.

6.1.3. Angular distributions
Finally, the angular-dependent slope distribution of a 2D surface profile can be obtained on the basis of equation (27) by changing variable to θ_m in accordance with equation (26):

Figure 9. Standard deviation of local slopes as a function of length scale ℓ over which it is defined for surfaces with following ACFs: (a) comparison of exponential and Gaussian ACFs as well as ACF of mounded surface ($\ell_0 = 35$ μm, $\ell_c = 25.6$ μm, $\Lambda = 220\mu$m, $\alpha = 0.1; 0.55; 0.9$); (b) ACF of self-affine surfaces with different values of Hurst exponent.
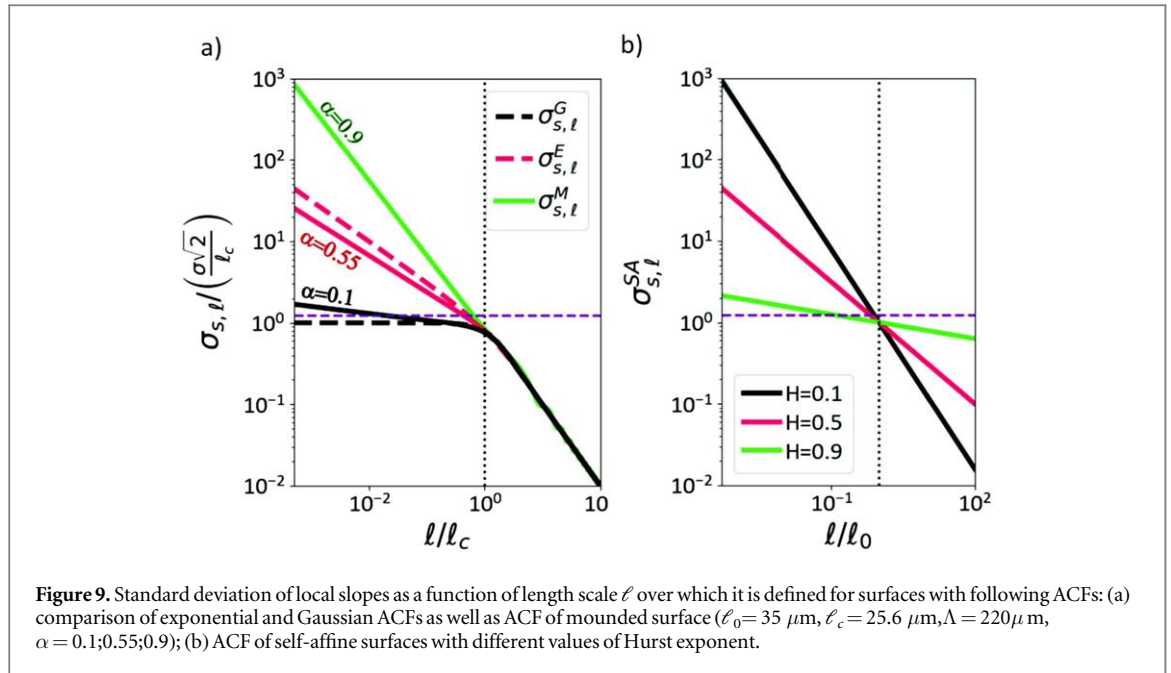
$$p_{2D}(\theta_m) = \frac{\tan \theta_m}{\sigma_{s,\ell}^2}(1 + \tan^2 \theta_m) \exp\left(-\frac{\tan^2 \theta_m}{2\sigma_{s,\ell}^2}\right),$$

(28)

where $\theta_m \in [0°, 90°]$—the angle between the normal to the facet surface and the normal to the mean surface.

In the case of 2D surface profile, the distribution of the slope angles $p_{2D}(\theta)$ reaches its maximum at a non-zero angle for any value of $\sigma_{s,l}$:

$$\tan \theta_{0,2D} = \sqrt{\frac{3\sigma_{s,\ell}^2 - 1 + \sqrt{4\sigma_{s,l}^2 + (1 - 3\sigma_{s,\ell}^2)^2}}{2}}.$$

(29)

$\theta_0 \leqslant 45°$.

Conversely the variance of slope distribution can be evaluated from the surface slope angular distribution using the inverse of equation (29):

$$\sigma_{s,\ell}^2 = \frac{\tan^2 \theta_{0,2D}(1 + \tan^2 \theta_{0,2D})}{1 + 3\tan^2 \theta_{0,2D}}.$$

(30)

6.2. Numerical computation of local slopes

In practice, the calculation of the local gradients along the x and y directions is the simplest way to evaluate the surface slopes from topography maps. Yet, this method is rather sensitive to the noise from experimental data and moreover it estimates the slopes at the lateral scale of the measurement step. Alternatively, it is possible to estimate the surface slopes at the scale of a surface element of size $\ell \times \ell$ by means of fitting a linear plane or a quadratic form. In this work, we compare these three methods (local gradient, linear or parabolic fits over a finite region of extent ℓ) while varying ℓ in the range 10–98 μm. Each surface element of the chosen characteristic size is fitted by the linear plane:

$$z = c_0 + c_x x + c_y y,$$

(31)

and by the quadratic expression:

$$z = a_0 + a_x x + a_y y + a_{xy} xy + a_{xx} x^2 + a_{yy} y^2.$$

(32)

In the latter case the plane tangent to the paraboloid at point (x_0, y_0) has the following c_x, c_y coefficients:

$$c_x = 2a_{xx}x_0 + a_{xy}y_0 + a_x,$$
$$c_y = a_{xy}x_0 + 2a_{yy}y_0 + a_y.$$

(33)

The unit normal vector to the plane describing this surface element $\mathbf{n}_s$ can be defined as:

$$\mathbf{n}_s = \frac{1}{\sqrt{c_x^2 + c_y^2 + 1}}(c_x, c_y, 1).$$

(34)

Finally, the polar angle θ and azimuthal angle ϕ describing the orientation of such surface element can be defined as dot products of $\mathbf{n}_s$ with unit vectors along z and x:

$$\cos \theta = \mathbf{n}_s \cdot \mathbf{n} = \frac{1}{\sqrt{c_x^2 + c_y^2 + 1}},$$

(35)

$$\tan \phi = \frac{c_y}{c_x}.$$

(36)

Applied to the whole topography map, such an analysis provides the full two-dimensional polar plot of the slope probability density function $p(s_{m,\ell})$. The one-dimensional representation is more convenient for the comparison of slope distributions of several samples. In case of isotropic surfaces this can be the radial average of the 2D polar plot of the slope probability density function. However, in a more general case of anisotropic surface a single 1D representation is not sufficient and at least two cuts through the 2D slope probability density function are necessary.

Table 4. Statistical estimators of the morphology of examined blasted aluminum samples: rms roughness σ, correlation length ℓ_c, functions $A(r)$ used for fitting the ACFs of the treated samples and their fit parameter ℓ_0, anti-correlation length ℓ_{ac}, characteristic length $2\pi/q_b$ corresponding to the breakpoint of PSD curves, curvature radii of trough-shaped craters r^c and dome-shaped hills r^h, variance of slope distribution σ_s (obtained from equation (23) using σ, ℓ_0 and α values from this table) and the slope angle θ_0 at which the slope angle distribution reaches its maximum (obtained from equation (29) using σ_s values from this table).

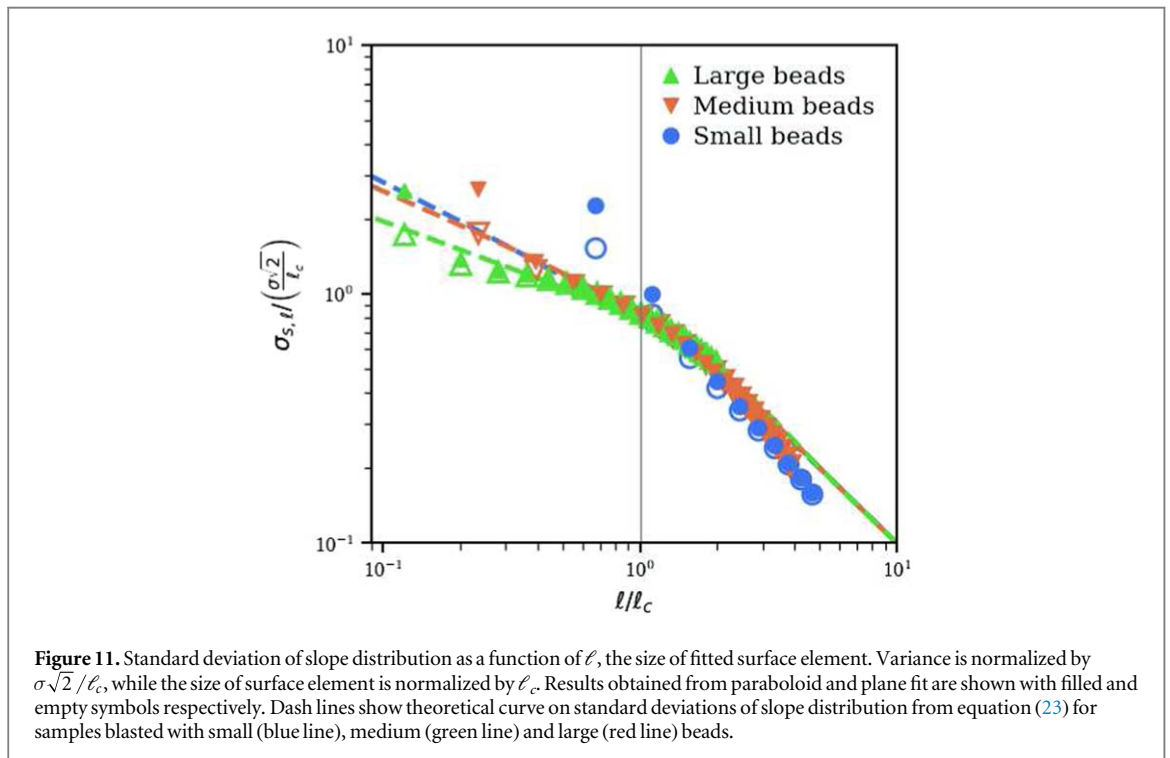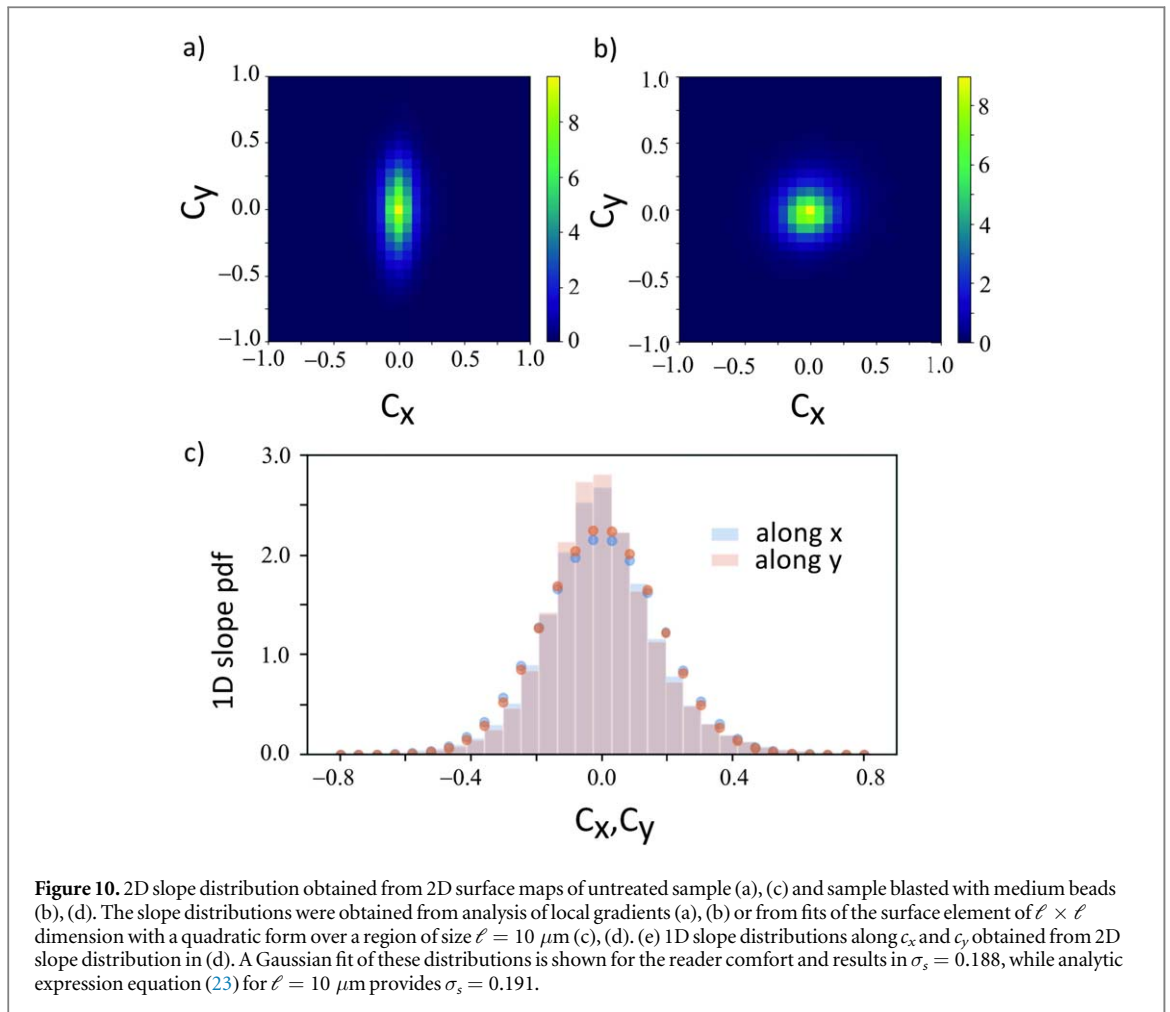|	Small beads	Medium beads	Large beads
$d_{beads}(\mu\text{m})$	70 ± 20	200 ± 50	500 ± 150
$\sigma(\mu\text{m})$	1.18 ± 0.04	2.52 ± 0.02	5.05 ± 0.06
$\ell_c(\mu\text{m})$	9.0 ± 0.3	25.6 ± 0.3	50.0 ± 0.7
$\mathcal{A}(\Delta r)$		$\exp\left[-\left(\frac{\Delta}{r}\ell_0\right)^{2\alpha}\right]\cos\left(\frac{2\pi r}{\Lambda}\right)$	
α (no units)	0.5	0.55	0.6
$\ell_0(\mu\text{m})$	11	30	80
$\Lambda(\mu\text{m})$	166	222	397
$\ell_{ac}(\mu\text{m})$	42.9 ± 3.8	78.2 ± 2.4	146.2 ± 4.5
$\widetilde{\mathcal{I}}_0(\mu\text{m}^3)$	25	251	1995
$2\pi/q_b(\mu\text{m})$	38	89	186
$1/c(\mu\text{m})$	85 ± 10	400 ± 10	872 ± 60
		based on statistical estimators	
σ_s	0.34	0.40	0.40
$\theta_0(°)$	21	25	25
		local slope analysis	
σ_s	0.31	0.27	0.25
$\theta_0(°)$	18.5	16	15

6.3. Experimental results

This section is devoted to the analysis of the slope distribution $p(s_{m,\ell})$ and of the distribution of the slope angles $p_{2D}(\theta_m)$ of the examined samples. Two approaches are compared: the analysis based on surface statistics (possible since the height distribution functions of the examined samples follow Gaussian statistics) and direct calculations from topography maps with a particular attention given to the impact of the length scale ℓ at which the surface elements are analyzed.
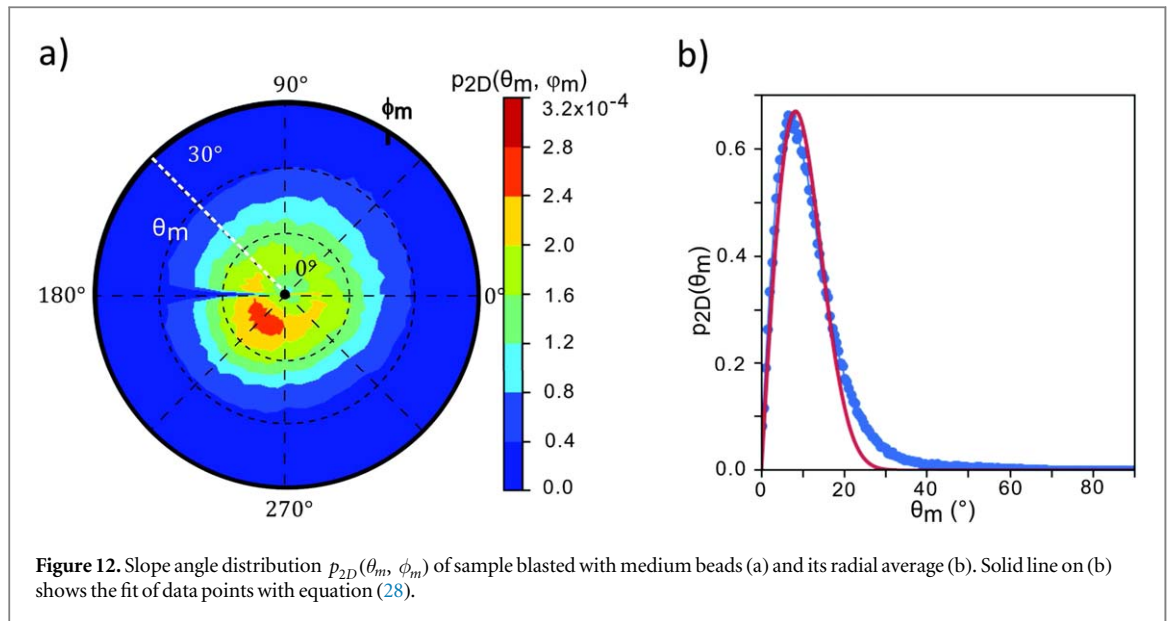
Based on the statistical parameters summarized in table 4, the standard deviation of the slope distribution σ_s was estimated using equation (23) for all three blasted samples and the following values were obtained for $\ell = 2\,\mu\text{m}$ ($\ell < \ell_0$, table 4): 0.34, 0.40 and 0.40 for samples blasted with small, medium and large beads, correspondingly. According to equation (29), slope angle θ_0 at which the slope angle distribution reaches its maximum is $\theta_0 = 21°$ for sample blasted with small beads, $\theta_0 = 25°$ for sample blasted with medium and large beads.

In what follows we will focus on the slope distributions $p(s_{m,\ell})$ and distributions of slope angles $p_{2D}(\theta_m)$ deduced from topography maps measured with optical profilometer and the results obtained in this way are presented in figure 2. Figure 10 shows such 2D slope distributions obtained for the untreated sample (figure 10(a)) and for sample blasted with medium beads (figure 10(b)). Slope distributions were obtained by fitting the surface element, the projection of which

to the mean surface plane is of size $\ell \times \ell = 10 \times 10\,\mu\text{m}$, with paraboloid equation (32) and defining the plane tangent to this paraboloid at the center of the surface element equation (33) (figures 10(c) and (d)). In fact, very similar results were obtained for fitting with plane and paraboloid. The slope distributions obtained from local gradients are, as expected, difficult to exploit due to the noise and aliasing, in contrast to the slope distributions obtained by fitting. The slope distribution of the untreated sample obtained by fitting 10(a) exhibit a clear anisotropy. Meanwhile, 2D slope distributions of all blasted samples have radial symmetry, as illustrated on figure 10(b) for sample blasted with medium beads. Figure 10(c) compares 1D cuts along $c_x = 0$ and $c_y = 0$ of the 2D slope distribution shown in figure 10(b) and is obtained from quadratic fits of height measurements on samples blasted with medium beads. The standard deviation of this slope distribution σ_s was estimated with equation (27) to be $\sigma_s = 0.188$, meanwhile analytic expression equation (23) for $\ell = 10\,\mu\text{m}$ provides $\sigma_s = 0.191$.

Figure 11 illustrates the variation of the standard deviation of the slope distribution $\sigma_{s,\ell}$ with the size ℓ of the fitted surface element. For the sake of comparison $\sigma_{s,\ell}$ values obtained for each sample are normalized by $\sigma\sqrt{2}/\ell_c$ similar to prefactor in equation (23). Results obtained from plane and quadratic fits are shown as filled and empty symbols, respectively. As expected, the increase of ℓ results in a more narrow slope distribution. Interestingly, for surface elements

Figure 10. 2D slope distribution obtained from 2D surface maps of untreated sample (a), (c) and sample blasted with medium beads (b), (d). The slope distributions were obtained from analysis of local gradients (a), (b) or from fits of the surface element of $\ell \times \ell$ dimension with a quadratic form over a region of size $\ell = 10$ μm (c), (d). (e) 1D slope distributions along c_x and c_y obtained from 2D slope distribution in (d). A Gaussian fit of these distributions is shown for the reader comfort and results in $\sigma_s = 0.188$, while analytic expression equation (23) for $\ell = 10$ μm provides $\sigma_s = 0.191$.

Figure 11. Standard deviation of slope distribution as a function of ℓ, the size of fitted surface element. Variance is normalized by $\sigma\sqrt{2}/\ell_c$, while the size of surface element is normalized by ℓ_c. Results obtained from paraboloid and plane fit are shown with filled and empty symbols respectively. Dash lines show theoretical curve on standard deviations of slope distribution from equation (23) for samples blasted with small (blue line), medium (green line) and large (red line) beads.

Figure 12. Slope angle distribution $p_{2D}(\theta_m, \phi_m)$ of sample blasted with medium beads (a) and its radial average (b). Solid line on (b) shows the fit of data points with equation (28).

of size $\ell \geqslant \frac{\ell_c}{2}$ the decay of $\sigma^2_{s,\ell}$ with ℓ/ℓ_c perfectly follows the law given by combination of equations (30) and (23). In conclusion, slope distributions of all blasted samples can be reasonably well approximated by the Gaussian form, which allows to use equation (23) for the analysis and to link the slope distribution with statistical properties like RMS and ℓ_c. Figure 12 shows 2D distributions of slope angles θ and ϕ obtained with equations (35), (36) from 2D slope distribution depicted by figure 10. Even though the slope distribution is Gaussian, due to normalization the distribution of slope angles is no more Gaussian and exhibits a maximum at $\theta_m \approx 7°$. A radial average of this distribution, shown on figure 12(b) follows well the expression given by equation (28).

In optical models based on the microfacet theory, there is one more morphology-related parameter, namely the shadowing/masking term [77, 78]. Yet, in contrast to the microfacet distribution, masking/shadowing can not be related to surface morphology in a simple and intuitive way. Analytic expressions for shadowing/masking exist for isotropic surfaces with Gaussian statistics [77, 78], but to the best of our knowledge, there is no convention on estimation of this parameter based directly on topography data.

6.4. Discussion on local surface slopes

As emphasized several times in this section, local slopes are to be defined with respect to a characteristic length scale [79](e.g. the wave length in the case of light scattering [80]). Here we could give a quantitative account of the size dependence of local slopes. In particular we could check that in the present case of Gaussian distribution of height fluctuations, the distribution of local slopes is also Gaussian and that its variance is fully determined by the knowledge of its auto-correlation function. As shown in figure 11 we observe that after rescaling by the correlation length

ℓ_c, all blasted samples show the same size dependence of the local slopes standard deviation. Since ℓ_c shows itself a quasi-linear dependence on the bead size, this means here that we get a full knowledge of the slope statistics from the process parameters
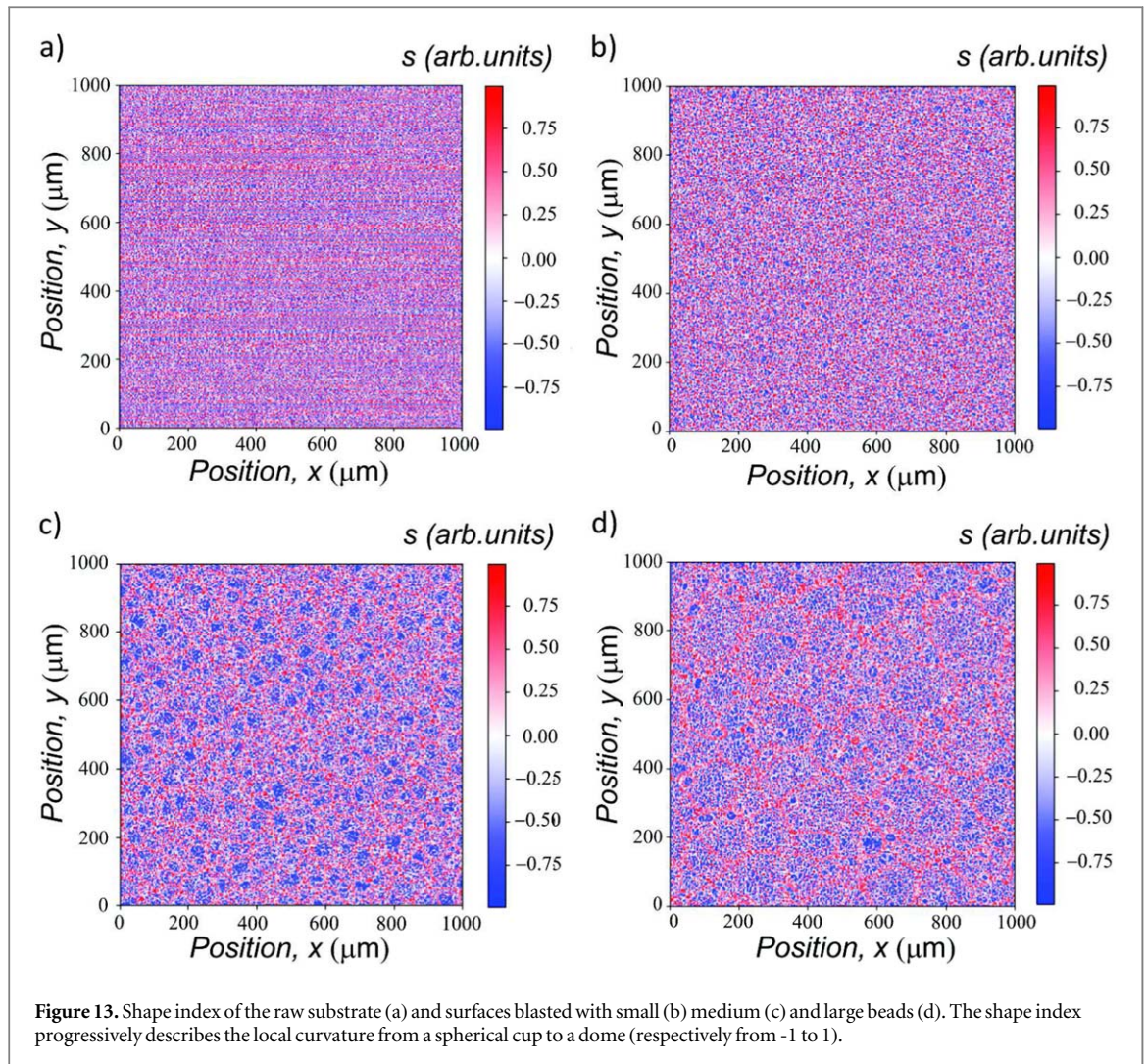
7. Local curvatures

7.1. Theoretical context

Two rather complementary approaches can be applied for characterization of local features of surface morphology: (i) distribution of all local curvatures and (ii) analysis of the shape and of the dimensions of statistically representative surface elements, as for instance hills and craters.

In order to emphasize the local curvature of the surface, topography maps can be presented through the *shape index*. This topography parameter was introduced by Koenderink & van Doorn [81] as the single valued measure of both principal local curvatures. Shape index is derived from the eigenvalues of the Hessian and can be described as follows:

$$s = \frac{2}{\pi} \arctan \frac{\kappa_1 + \kappa_2}{\kappa_2 - \kappa_1} \quad (37)$$

where $\kappa_1 = \max\left(\frac{\partial^2}{\partial x^2}h(x, y); \frac{\partial^2}{\partial y^2}h(x, y)\right)$ and $\kappa_2 = \min\left(\frac{\partial^2}{\partial x^2}h(x, y); \frac{\partial^2}{\partial y^2}h(x, y)\right)$. The scale of shape index values is set from -1 to 1 and progressively describes the local curvature from a spherical cup $s \in [-1; -\frac{7}{8}]$, to a trough $s \in \left[-\frac{7}{8}; -\frac{5}{8}\right]$, a rut $s \in \left[-\frac{5}{8}; -\frac{3}{8}\right]$, a saddle rut $s \in \left[-\frac{3}{8}; -\frac{1}{8}\right]$, a saddle $s \in \left[-\frac{1}{8}; \frac{1}{8}\right]$, a saddle ridge $s \in \left[\frac{1}{8}; \frac{3}{8}\right]$, a ridge $s \in [\frac{3}{8}; \frac{5}{8}]$, a dome $s \in [\frac{5}{8}; \frac{7}{8}]$ and a spherical cap $s \in \left[\frac{7}{8}; 1.0\right]$. While the shape index is independent of the size of the surface element it describes, this information can be retrieved from curvedness

Figure 13. Shape index of the raw substrate (a) and surfaces blasted with small (b) medium (c) and large beads (d). The shape index progressively describes the local curvature from a spherical cup to a dome (respectively from -1 to 1).

parameter c [81]:

$$c = \sqrt{\frac{\kappa_1^2 + \kappa_2^2}{2}} \qquad (38)$$

Curvedness is always positive and is inversely proportional to the size of surface element. Finally, the probability density function of shape index gives the qualitative insight on its statistics in a similar way as the height distribution function describes the height profile.

The analysis of the average dimensions of local features, such as craters and hills in this work, can also be useful. The suggested procedure is as follows. By combining the shape index map and the curvedness map, the curvedness pdf is calculated for each shape of interest, i.e. spherical cup and trough or ridge.
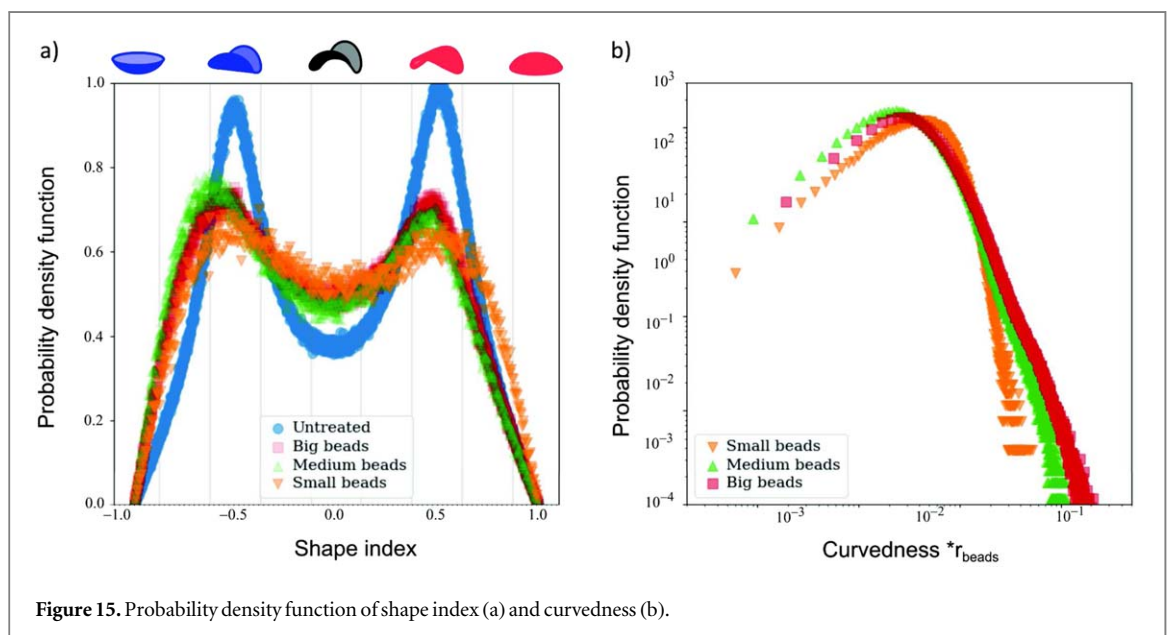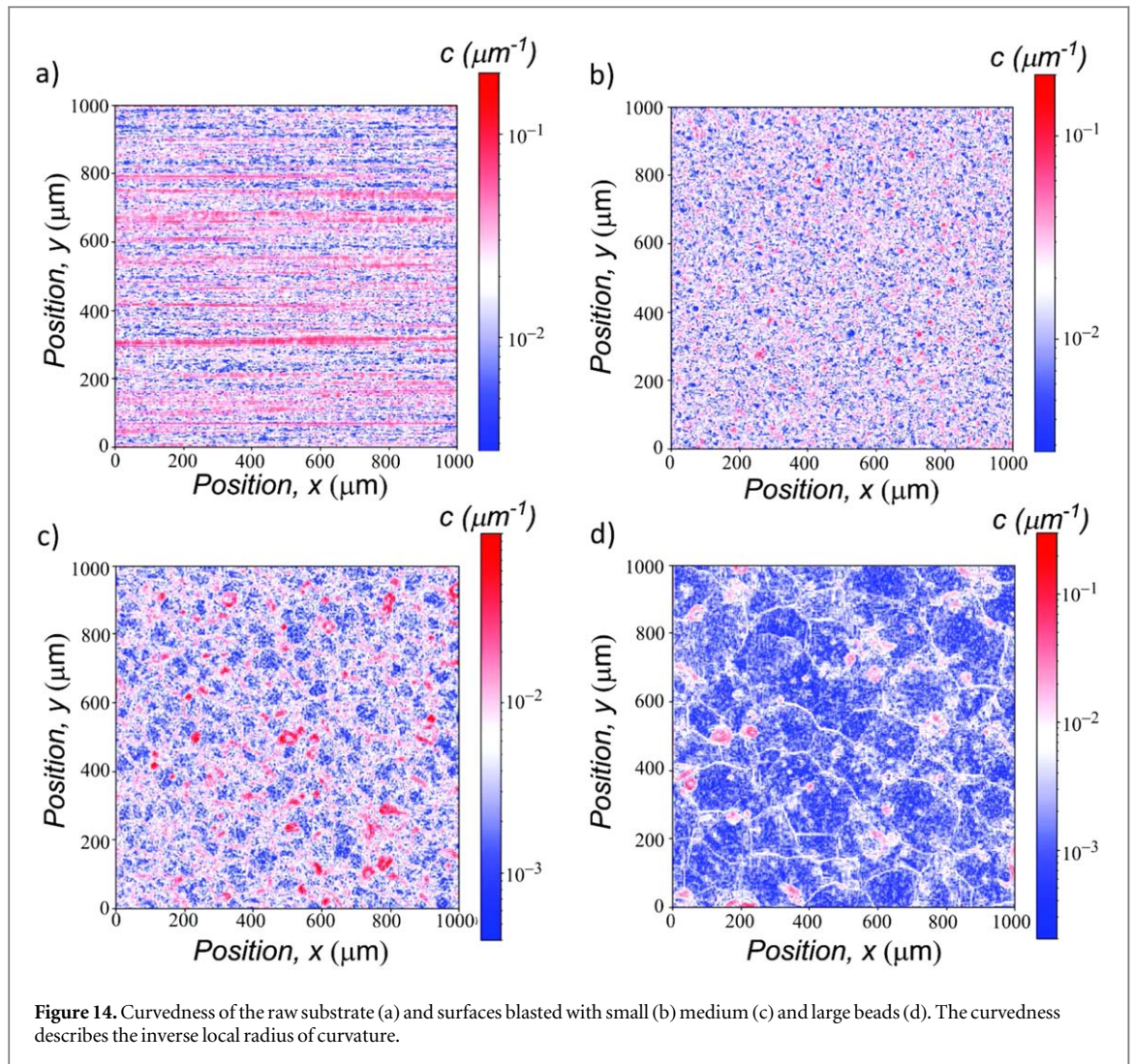
7.2. Experimental results

Obviously, in full analogy with the local slopes, the analysis of local curvatures can not be performed disregarding the characteristic length-scales of the surface. Due to the important scale-dependence of the local properties of mounded surfaces examined in this work, the shape index and curvedness calculations

provided were obtained from height maps depicted in figure 2.

Figure 13 provides a shape index representation of topography maps from figure 2 and thus allows us to analyze the local curvature shapes of the surface. Shape index values were calculated with shape_index function from scikit-image python library for image processing. According to figure 13, spherical cup shapes corresponding to the craters induced by the blasting process are dominant on the surface of examined samples. Those craters are surrounded by crests described by small positive local curvatures. Finally, the intersection between several crests results in local maxima (dome-like shape).

Figure 15(a) shows the probability density function of shape index, s. It reveals that the surface of non-treated sample is predominantly composed of two types of surface curvature elements: ruts ($s = -0.5$) and ridges ($s = 0.5$). Then blasting with small beads results in roughly equal amount of surface points belonging to shapes from rut to ridge. Blasting with medium and large beads renders the probability density of shape index asymmetric: troughs ($s = -0.75$, intermediate case between cup-like shape and rut)

Figure 14. Curvedness of the raw substrate (a) and surfaces blasted with small (b) medium (c) and large beads (d). The curvedness describes the inverse local radius of curvature.

Figure 15. Probability density function of shape index (a) and curvedness (b).

become dominant and occupy more important surface than ridges.

Figure 14 shows the maps of curvedness, c. Then figure 15(b) plots the probability density curvedness

times beads radius of all blasted samples. Among examined samples rolled aluminum has largest predominant curvedness of $1.3 \cdot 10^{-2}$ μm^{-1}, while in blasted samples this value decreases with the beads size and is

$1.18.\,10^{-3}\ \mu\mathrm{m}^{-1}$, $2.5.\,10^{-3}\ \mu\mathrm{m}^{-1}$ and $1.16.\,10^{-3}\ \mu\mathrm{m}^{-1}$ for aluminum samples blasted with small, medium and large beads respectively. The corresponding radii of curvature of blasted samples are 85 μm, 400 μm and 862 μm for small, medium and large beads respectively.

The summary of the different statistical estimators examined in this work is given in table 4.

7.3. Discussion on local curvatures

In addition to its quantitative interest, the analysis of local curvatures brings an additional topological information to the present topographic characterization of blasted aluminum surfaces. The maps and the statistics of the shape index show a spectacular change between the initial groove geometry of the initial cold-rolled surfaces and the crater geometry of the blasted surfaces. In particular a clear asymmetry appears in the distribution of shape indices between the bottoms and the ridges of the craters. Such an asymmetry could not be captured by the correlation or the slope analysis. Moreover the local curvature analysis appears to be far more robust than the fragile estimation of the skewness.

8. Conclusion and outlook

A detailed statistical study of the surface topography of blasted aluminum samples was performed. Combining three different experimental facilities for measurement of surface topography allowed for characterization of surface topography of the samples within 5 decades of spatial frequency. Several statistical morphological parameters were extracted from the experimental data during their analysis. Within the examined range of beads sizes used during the blasting process of the sample, the value of the RMS height of the rough surface is found to increase linearly with the size of the beads. The obtained values of the skewness and the kurtosis both reflected slight deviations of the height distribution from a Gaussian form, consistent with the presence of 'blasting' craters on the surface. The PSD allows us to identify the size of the beads used during the fabrication process. The spatial length scales over which the empirical ACFs display anti-correlations are related to the sizes of the beads impacting the surface. Interestingly, while the large scale roughness appears to be controlled by the blasting process, we could show that the microscale roughness inherits from that of the initial samples. We could show that the slope statistics is fully characterized by the knowledge of the quasi-Gaussian distribution of height fluctuations and of the auto-correlation functions. On the one hand, local slopes are shown to be strongly dependent on the length scale. On the other hand, after a proper rescaling by the bead size, the slope distributions of the studied surfaces are all very similar for all three blasted samples.

This study creates a solid foundation for future work on understanding the light scattering from these blasted surfaces and how it is related to their surface topographies. For instance, the experimental topography data analyzed in this work will be used as an input into different light scattering models that will produce scattering data that can be confronted to optical experimental data, in order to evaluate their practical application.

Data availability statement

The data that support the findings of this study are available upon reasonable request from the authors.

ORCID iDs

J Cabrero ⬤ https://orcid.org/0000-0002-4244-3382
I Simonsen ⬤ https://orcid.org/0000-0002-4244-3382
D Vandembroucq ⬤ https://orcid.org/0000-0002-1639-5284
I Gozhyk ⬤ https://orcid.org/0000-0002-8287-307X

References

[1] Feng L, Li S, Li Y, Li H, Zhang L, Zhai J, Song Y, Liu B, Jiang L and Zhu D 2002 Super-hydrophobic surfaces: from natural to artificia *Adv. Mater.* **14** 1857
[2] Persson B N J 2014 Theory of rubber friction and contact mechanics *J. Chem. Phys.* **115** 3840–61
[3] Pastewka L and Robbins M O 2014 Contact between rough surfaces and a criterion for macroscopic adhesion *PNAS* **111** 3298–303
[4] Stover J C 2012 *Optical Scattering: Measurement and Analysis* 3rd edn (Bellingham, Wash: SPIE Press) (https://doi.org/10.1117/3.975276)
[5] Zhai C, Hanaor D, Proust G, Brassart L and Gan Y 2016 Interfacial electro-mechanical behaviour at rough surfaces *Extreme Mechanics Letters* **9** 422–9
[6] Zhai C, Gan Y, Hanaor D, Proust G and Retraint D 2016 The role of surface structure in normal contact stiffness *Exp. Mech.* **56** 359–68
[7] Rayleigh L 1907 On the dynamical theory of gratings *Proc. R. Soc. London Ser.* A **79** 399–416
[8] Chenmoganadam T K 1919 On the specular reflection from rough surfaces *Phys. Rev.* **13** 96–101
[9] Duparre A, Ferre-Borrull J, Gliech S, Notni G, Steinert J and Bennett J M 2002 Surface characterization techniques for determining the root-mean-square roughness and power spectral densities of optical components *Appl. Opt.* **41** 154–71
[10] Elson J M and Bennett J M 1979 Relation between the angular dependence of scattering and the statistical properties of optical surfaces *J. Opt. Soc. Am.* **69** 31–47

[11] Elson J M and Bennett J M 1995 Calculation of the power spectral density from surface profile data *Appl. Opt.* **34** 201–8

[12] Beckmann P and Spizzichino A 1963 *The Scattering of Electromagnetic Waves from Rough Surfaces* (Oxford: Pergamon Press)

[13] Phong B T 1975 Illumination for computer generated pictures *Commun. ACM* **18** 311–7

[14] Blinn J F 1977 Models of light reflection for computer synthesized pictures *Proceeding SIGGRAPH* pp 192–8

[15] Walter B, Marschner R S, Li H and Torrance K E 2007 Microfacet models for refraction through rough surfaces *Proc. Eurographics* **1** 195–206

[16] Cook R L and Torrance K E 1982 A reflectance model for computer graphics *ACM Trans. Graph.* **1** 7–24

[17] Ashikhmin M and Shirley P S 2000 An anisotropic phong BRDF model *Journal of Graphics Tools* **5** 25–32

[18] Schlick C 1994 An inexpensive BRDF model for physically-based rendering *Comput. Graphics Forum* **13** 233–46

[19] Nakano T and Tamagawa Y 2005 Physically based reflectance model utilizing polarization measurement *Appl. Opt.* **44** 2957–62

[20] Yan L Q, Hasan M, Walter B, Marschner S and Ramamoorthi R 2018 Rendering specular microgeometry with wave optics *ACM Trans. Graph.* **37** 1–10

[21] Turbil C, Yoo T S H, Simonsen I, Teisseire J, Gozhyk I and Garcia-Caurel E 2019 Experimental studies of the transmission of light through low coverage regular or random arrays of silica micropillars supported by a glass substrate *Appl. Opt.* **58** 9267–78

[22] Krywonos A, Harvey J E and Choi N 2011 Linear systems formulation of scattering theory for rough surfaces with arbitrary incident and scattering angles *J. Opt. Soc. Am.* A **28** 1121–38

[23] Simonsen V P, Bedeaux D and Simonsen I 2021 Nonparametric reconstruction of the statistical properties of penetrable, isotropic randomly rough surfaces from in-plane, co-polarized light scattering data: application to computer generated and experimental scattering data *Phys. Rev.* **104** 043502

[24] Simonsen I, Hetland Ø S, Kryvi J B and Maradudin A A 2016 Determination of the normalized surface height autocorrelation function of a two-dimensional randomly rough dielectric surface by the inversion of light scattering data *Phys. Rev.* A **93** 043829

[25] Wensink H, Schlautmann S, Goedbloed M H and Elwenspoek M C 2002 Fine tuning the roughness of powder blasted surfaces *J. Micromech. Microeng.* **12** 616–20

[26] Slatineanu L, Potarniche S, Coteaja M, Grigoras (Besliu) I, Gherman L and Negoescu F 2011 Surface roughness at aluminium parts sand blasting *Proceedings in Manufacturing Systems* **6** 69–74

[27] Rudawska A, Danczak I, Müller M and Valasek P 2016 The effect of sandblasting on surface properties for adhesion *Int. J. Adhes.* **70** 176–90

[28] Sosale G, Hacking S A and Vengallatore S 2008 Topography analysis of grit-blasted and grit-blasted-acid-etched titanium implant surfaces using multi-scale measurements and multi-parameter statistics *J. Mater. Res.* **23** 2704–13

[29] Marteau M, Bigerelle M, Mazeran P E and Bouvier S 2015 Relation between roughness and processing conditions of AISI 316L stainless steel treated by ultrasonic shot peening *Tribol. Int.* **82** 319–29

[30] Xia Y, Bigerelle M, Bouvier S, Iost A and Mazeran P E 2015 Quantitative approach to determine the mechanical properties by nanoindentation test: application on sandblasted materials *Tribol. Int.* **82** 297–304

[31] Todd D R H, Allen D K and Alting L 1994 *Manufacturing Processes Reference Guide* 4th edn (Industrial Press)

[32] Finnie I 1960 Erosion of surfaces by solid particles *Wear* **3** 87–103

[33] Kleis I and Kulu P 2008 *Solid Particle Erosion: Occurrence, Prediction and Control* (London: Springer-Verlag)

[34] Verma A P and Lal G K 1979 An experimental study of abrasive jet machining *Int J Math Tool Des Rcs* **2** 19–29

[35] Carter G, Bevan J, Katardjiev I V and Nobes M J 1991 The erosion of copper by reflected sandblasting grains *Mater. Sci. Eng.* A **132** 231–6

[36] Thomas T R 1999 *Rough Surfaces* 2nd edn (London: Imperial College Press)

[37] Ourahmoune R, Salvia M, Mathia T G and Mesrati N 2014 Surface morphology and wettability of sandblasted PEEK and its composites *Scanning* **36** 64–75

[38] Bartkowiak T, Berglund J and Brown C A 2018 Establishing functional correlations between multiscale areal curvatures and coefficients of friction for machined surfaces *Surf. Topogr.: Metrol. Prop.* **6** 034002

[39] Zhao Y, Wang G-C and Lu T-M 2001 Characterization of amorphous and crystalline rough surface principles and applications *Experimental Methods in the Physical Sciences* vol **37** 26–59

[40] Dong W P, Sullivan P J and Stout K J 1994 Comprehensive study of parameters for characterising three-dimensional surface topography: III: Parameters for characterising amplitude and some functional properties *Wear* **178** 29–43

[41] Dong W P, Sullivan P J and Stout K J 1994 Comprehensive study of parameters for characterising three-dimensional surface topography: IV: Parameters for characterising spatial and hybrid properties *Wear* **178** 45–60

[42] Brown C A *et al* 1992 Multiscale analyses and characterizations of surface topographies *CIRP Ann.* **67** 839–62

[43] Ho H S, Bigerelle M, Vincent R and Deltomb R 2016 MCorrelation modeling between process condition of sandblasting and surface texture: A multi-scale approach *Scanning* **38** 191–201

[44] Plouraboué F and Boehm M 1999 Multi-scale roughness transfer in cold metal rolling *Tribol. Int.* **32** 45–7

[45] Vandembroucq D, Tarrats A, Greffet J J, Roux S and Plourabou F 2001 Light scattering from cold rolled aluminium surfaces *Opt. Comm.* **187** 289–94

[46] Milanese E, Brink T and Aghababaei R 2019 Emergence of self-affine surfaces during adhesive wear *Nat. Commun.* **10** 1116

[47] Dong W P, Sullivan P J and Stout K J 1993 Comprehensive study of parameters for characterizing three-dimensional surface topography II: statistical properties of parameter variation *Wear* **167** 9–21

[48] Church E L and Takacs P Z 1995 Surface scattering *Handbook of Optics* **1** 7–1

[49] Akarapu S, Sharp T and Robbins M O 2011 Stiffness of contacts between rough surfaces *Phys. Rev. Lett.* **106** 204301

[50] Mandelbrot B, Passoja D and Paullay A 1984 Fractal character of fracture surfaces of metals *Nature* **308** 721–2

[51] Church E L and Takacs P Z 1991 Effects of non-vanishing tip size in mechanical profile measurements *Proc. SPIE* **1332** 504–14

[52] Wu J-J 2000 Spectral analysis for the effects of stylus tip curvature on measuring fractal profiles *Meas. Sci. Technol.* **11** 1369

[53] Nečas D, Valtr M and Klapetek P 2020 How levelling and scan line corrections ruin roughness measurement and how to prevent it *Sci Rep.* **10** 15294

[54] Simonsen I 2010 Optics of surface disordered systems: a random walk through rough surface scattering phenomena *Eur. Phys. J. Special Topics* **181** 1–103

[55] Yaglom A M 1987 Correlation theory of stationary and related random functions I *Basic Results* (Berlin: Springer-Verlag)

[56] Dong W P, Sullivan P J and Stout K J 1992 Comprehensive study of parameters for characterizing three-dimensional surface topography I: Some inherent properties of parameter variation *Wear* **159** 161–71

[57] Agarwal R A, Patki G S and Basu S K 1979 An analysis of surface profiles for stationarity and ergodicity *Precis. Eng.* **1** 159–65

[58] Grabon W and Pawlus P 2014 Description of two-process surface topography *Surf. Topography: Metrol. Prop.* **2** 025007

[59] Ogilvy J A 1991 *Theory of Wave Scattering From Random Rough Surfaces* (Bristol: IOP Publishing)

[60] Persson B N J, Albohr O, Tartaglino U, Volokitin A I and Tosatti E 2005 On the nature of surface roughness with application to contact mechanics, sealing, rubber friction and adhesion *J. Phys.: Condens. Matter* **17** R1–62

[61] L'vov V S, Podivilov E, Pomyalov A, Procaccia I and Vandembroucq D 1998 Improved shell model of turbulence *Phys. Rev.* E **58** 1811–22

[62] King T G 1980 rms skew and kurtosis of surface profile height distributions: some aspects of sample variation *Precis. Eng.* **2** 207–15

[63] Vorburger T V, Rhee H G, Renegar T B, Song J-F and Zheng A 2007 Comparison of optical and stylus methods for measurement of surface textures *Int. J. Adv. Manuf. Technol.* **33** 110–8

[64] Kundrak J, Gyani K and Bana V 2008 Roughness of ground and hard-turned surfaces on the basis of 3D parameters *Int. J. Adv. Manuf. Technol.* **38** 110–9

[65] Lechenault F, Pallares G, George M, Rountree C L, Bouchaud E and Ciccotti C 2010 Effects of finite probe size on self-affine roughness measurements *Phys. Rev. Lett.* **104** 025502

[66] ISO 25178

[67] Grossman E N, Gould M and Mujica-Schwann N P 2016 Robust evaluation of statistical surface topography parameters using focus-variation microscopy *Surf. Topogr.: Metrol. Prop.* **4** 035003

[68] Pelliccione M and Lu T-M 2008 *Evolution of Thin Film Morphology* (Berlin, Heidelberg: Springer-Verlag)

[69] Simonsen I, Vandembroucq D and Roux S 2000 Wave scattering from self-affine surfaces *Phys. Rev.* E **61** 5914–7

[70] Simonsen I, Vandembroucq D and Roux S 2001 Electromagnetic wave scattering from conducting self-affine surfaces: an analytic and numerical study *J. Opt. Soc. Am.* A **18** 2001

Simonsen I, Vandembroucq D and Roux S 2001 Electromagnetic wave scattering from conducting self-affine surfaces: an analytic and numerical study *J. Opt. Soc. Am.* A **18** 1101–11

[71] Strand D, Nesse T, Kryvi J B, Hegge T S and Simonsen I 2018 Wave scattering from two-dimensional self-affine Dirichlet and Neumann surfaces and its application to the retrieval of self-affine parameters *Phys. Rev.* A **97** 063825

[72] Persson B N J 2014 On the fractal dimension of rough surfaces *Tribol. Lett.* **54** 99–106

[73] Papoulis A 1977 *Signal Analysis* (New York: McGraw-Hill)

[74] Jacobs T D B, Junge T and Pastewka L 2017 Quantitative characterization of surface topography using spectral analysis *Surf. Topogr.: Metrol. Prop.* **5** 013001

[75] Jones K H 1998 A comparison of algorithms used to compute hill slope as a property of the DEM *Comput. Geosci.* **24** 315–23

[76] Maloy K J, Hansen A, Hinrichsen E L and Roux S 1992 Experimental measurements of the roughness of brittle cracks *Phys. Rev. Lett.* **68** 213

[77] Smith B G 1967 Geometrical shadowing of a random rough surface *IEEE T. Antenn. Propag.* **15** 668–71

[78] Heitz E, Hanika J, d'Eon E and Dachsbacher C 2016 Multiple-scattering microfacet BSDFs with the smith model *ACM Trans. Graph* **35** 1–14

[79] Lopez J, Hansali G, Zahouani H, Le Bosse J C and Mathia T 1995 3D fractal-based characterisation for engineered surface topography *Int. J. Mach. Tools Manuf* **35** 211–7

[80] O'Donnell K A and Mendez E R 1987 Experimental study of scattering from characterized random surfaces *J. Opt. Soc. Am.* A **4** 1194–205

[81] Koenderink J J and Van Doorn A J 1992 Surface shape and curvature scales *Image Vision Comput.* **10** 557–64